

NORTHWESTERN UNIVERSITY

Uncovering the Origins of the Binding Properties
of Spherical Nucleic Acids

A DISSERTATION

SUBMITTED TO THE GRADUATE SCHOOL
IN PARTIAL FULLFILLMENT OF THE REQUIREMENTS

for the degree

DOCTOR OF PHILOSOPHY

Field of Chemistry

By

Lam-Kiu Fong

EVANSTON, ILLINOIS

September 2018

© Copyright by Lam-Kiu Fong, 2018

All Rights Reserved

ABSTRACT

Uncovering the Origins of the Binding Properties of Spherical Nucleic Acids

Lam-Kiu Fong

Spherical nucleic acids (SNAs) are a class of structures composed of spherical nanoparticle cores that are densely functionalized with radially oriented, linear DNA. SNAs exhibit properties that are distinct from those of their linear counterparts. These constructs can readily enter cells, evade nuclease degradation, and bind complementary DNA targets with binding constants orders of magnitude larger than those of linear DNA of the same sequence. These fundamentally interesting properties have led to the use of SNAs as medical diagnostic probes, gene regulation agents, and building blocks for programmable colloidal crystal engineering. The unifying property that enables the application of SNAs in all of these fields is their ability to bind complementary DNA sequences with a higher affinity constant than linear DNA. Despite how essential this binding property is to the practical implementation of SNAs, little is known about its origin and how it changes with the SNA architecture, e.g. nanoparticle shape and DNA surface density.

This thesis answers fundamental questions about how the architecture of DNA-nanoparticle conjugates affects their ability to bind complementary DNA, and what considerations should be taken in order to move beyond the spherical architecture of SNAs in order to use optically interesting anisotropic cores. In Chapter 2, the difference between linear DNA hybridization and hybridization to a DNA-functionalized spherical nanoparticle was explored. Hybridization onto DNA-functionalized particles is shown to be enthalpically enhanced due to the structural

confinement of the DNA duplex on the surface. This confinement prevents DNA from adopting conformationally unfavorable states, and is further enhanced by high DNA surface density. This understanding challenges the idea that molecular crowding is detrimental to duplex formation, and led us to investigate the effect of DNA surface density and nanoparticle radius of curvature on the types of DNA displacement reactions that govern the efficacy of SNA-based intracellular detection probes. The work in Chapter 3 shows that when a complementary DNA strand is tightly bound to a densely functionalized spherical particle, the propensity for displacement is highly tunable with nanoparticle size. The size of the spherical nanoparticle was varied to demonstrate that complementary DNA strands are more weakly bound on large nanoparticles and displacement is therefore more favorable. The enthalpy of hybridization can be varied by 10-20 kcal/mol simply by changing the SNA architecture (e.g., particle size and DNA surface density) without ever modifying the DNA sequence. This result emphasizes the idea that moving to anisotropic nanoparticle cores, which are larger and have a smaller radius of curvature than spherical nanoparticles, imparts DNA-nanoparticle conjugates with a knob of binding tunability that is independent of the DNA shell. Finally, one limitation to the implementation of anisotropic DNA-functionalized cores is the ability to synthesize certain anisotropic nanoparticles uniformly and in high yields. In Chapter 4, the mechanism of formation of anisotropic gold triangular prisms was studied to understand why reaction conditions favor a broad product distribution. Nanoparticle probes of varying chemical and structural compositions were used to test the hypothesis that prisms form by heterogeneous nucleation. Interestingly, triangular prisms form by homogenous nucleation, in stark contrast to the accepted heterogeneous nucleation pathway. This finding creates a route for the optimization of synthesis yields, because it indicates that to

improve product yield and uniformity for some anisotropic nanoparticle shapes, efforts should be placed toward studying reaction conditions that promote homogenous nucleation.

This work demonstrates that fundamental knowledge of DNA hybridization thermodynamics on SNAs and nanoparticle synthesis specifically addresses limitations to the construction and implementation of anisotropic DNA-nanoparticle conjugates. Chapter 5 summarizes these findings and points to several future directions for this research area.

Thesis Advisors: Professor Chad A. Mirkin and Professor George C. Schatz

ACKNOWLEDGEMENTS

Throughout the last six years of my Ph.D. I have become a more critical and independent thinker and have found a passion for science I didn't even realize I had. This journey would not have been nearly as rewarding had it not been for the community of people who uplift me, encourage me and listen to my ideas on a daily basis.

First and foremost, I would like to thank my mom, Sandra, for sacrificing everything so that I would have the opportunity to excel, for teaching me how to question and be heard, and for all of the love, encouragement, patience and joy she has given me since the day I was born. And for all of the laughter, Gracias!

To my wonderful partner, Kevin. Thank you for believing in me and in us. Thank you for being my most objective critic and my most subjective supporter. Sharing ideas with you has made all the difference. To many great years of life and science together.

To my brother, Gabriel, and my sister, Kaylee, whose creativity and wonder inspire me to be curious in all of my endeavors.

To my stepdad Aldo, whose whimsical approach to life has given me perspective on the most stressful days.

To my friends, thank you for being my family. To Amanda and Brandon, for all of the fun adventures we took together and for getting me through the qualifying exam. To the lady scientists that inspire me, Kavita, Linda, Niki, Katie. To my friends who helped and encouraged me to make a difference, Kedy, Dana Alicia. To the best lab friends and real friends who make coming to lab worth every minute, Andrea, Lisa, JT, Mike Ashley, Christine, Oliver, Eileen, Matt O'Brien, Lin, Jeff, Keith, Dan, Chad Shade, Jessie and Tuncay.

To my mentors, Kevin Kohlsiedt who taught me how to use a computer to do science, and Matt Jones who taught me how to give a scientific presentation and design control experiments.

To all of the faculty who have supported my diversity initiatives, Regan Thompson, Emily Weiss, Peter Stair. We are making a change.

To Jonathan, Laura and Madison for always looking out.

Finally, I would like to thank my advisors: Chad, thank you for always encouraging me to be more critical of my work and my ideas, and for spending so much time helping me learn how to write. George, thank you for always making the time to talk through difficult problems and for your general enthusiasm toward my work.

Thanks for an amazing six years!

TABLE OF CONTENTS

ABSTRACT	3
ACKNOWLEDGEMENTS	6
LIST OF TABLES AND FIGURES	12
CHAPTER 1: INTRODUCTION: UNDERSTANDING THE STRUCTURE-FUNCTION RELATIONSHIP OF DNA-NANOPARTICLE CONJUGATES.....	16
1.1 Summary	17
1.2 DNA Nanoparticle Conjugates: Their Properties and Applications	18
1.2.1 Introduction to Spherical Nucleic Acids	18
1.2.2 Core-Independent Properties of SNAs	19
1.2.3 Applications of SNAs.....	23
1.3 Introduction to Thesis Topics: Understanding the Effect of SNA Architecture on Binding	28
1.3.1 Explaining the Origin of Enhanced Binding on SNAs.....	29
1.3.2 The Role of Radius of Curvature on DNA Displacement Reactions on SNAs.....	30
1.3.3 Elucidating the Mechanism of Gold Nanoprism Formation to Improve Reaction Yield.....	30
CHAPTER 2: THE ROLE OF STRUCTURAL ENTHALPY IN SPHERICAL NUCLEIC ACID HYBRIDIZATION.....	31
2.1 Summary	31
2.2 Introduction	33
2.3 Results and Discussion	34
2.3.1 Binding Enhancement Onto SNAs is Confirmed by Concentration-Dependent Fluorescence Hybridization Experiments.....	34
2.3.2 Isothermal Titration Calorimetry Confirms that Hybridization Enthalpy on SNAs is More Favorable Than in the Linear Case.....	38
2.3.3 Coarse-Grained Molecular Dynamics Simulations Demonstrate that the Enthalpic Binding Enhancement Observed on SNAs Results From Structural Confinement of the DNA	44

2.3.4 Less confined SNA Architectures Have Less Favorable Enthalpy of Hybridization in Support of the Structural Confinement Hypothesis.....	50
2.3.5 The large entropic cost incurred upon complementary strand hybridization to SNAs is also explained by structural confinement	52
2.4 Conclusions	53
2.5 Experimental Methods.....	54
2.5.1 DNA and SNA Synthesis and Purification.....	54
2.5.2 DNA Density Quantification on SNAs	54
2.5.3 Fluorescence Hybridization Experiments.....	55
2.5.4 Treatment of the SNA as Single Entity for Analysis.....	55
2.5.5 Isothermal Titration Calorimetry Experiments.....	56
2.5.6 Simulation Model and Systems	57
2.5.7 Implicit-Ion Simulations Method	58
2.5.8 Melting Curve Calculated from Implicit-Ion Simulations	58
2.5.9 Calculation of Hybridization Enthalpy in Implicit-Ion Simulations	60
2.5.10 Explicit-Ion Simulation Model and Procedure.....	60
2.5.11 Calculation of Hybridization Enthalpy in Explicit-Ion Simulations	61
CHAPTER 3: THE ROLE OF SURFACE ATTACHMENT ON THE ENTHALPY OF DNA	
DISPLACEMENT REACTIONS	62
3.1 Summary	63
3.2 Introduction	64
3.3 Results and Discussion	64
3.3.1 Linear DNA Experiment Reveals the Feasibility of Using ITC to Study Displacement Reactions	64
3.3.2 SNA Displacement Experiments Confirm Binding Enhancement Relative to Linear DNA	67
3.3.3 The Versatility of the SNA Architecture in Directing Displacement Reactions is Tested.....	68
3.3.4 Determining of the Role of Radius of Curvature on Displacement Reactions from SNAs	69
3.4 Conclusions	71

CHAPTER 4: UNDERSTANDING THE NANOPARTICLE-MEDIATED NUCLEATION PATHWAYS OF ANISOTROPIC NANOPARTICLES.....	72
4.1 Summary	73
4.2 Introduction	74
4.3 Results and Discussion	79
4.3.1 Changes in Nanoparticle Precursor Size and Defect Structure do not Preclude Formation of Prisms	79
4.3.2 Successful Synthesis of Prisms with Quantum Dot Precursors Suggest a Homogeneous Nucleation Mechanism.....	80
4.3.3 Prism Synthesis with Palladium Nanoparticles Reveals that the Nanoparticle Precursor Templates the Spherical Impurity Products	82
4.3.4 The Nanoparticle Precursor Plays a Dual Catalytic and Templating Role in the Synthesis of Gold Triangular Nanoprisms	83
4.3.5 Nanoparticle Shape is Used as a Handle to Test and Confirm the Mechanism of Gold Nanoprism Nucleation.....	86
4.4 Conclusions	87
4.5 Experimental Methods	88
4.5.1 Prism Growth Solution Preparation.....	88
4.5.2 Nanoparticle Precursor Concentration Determination	89
4.5.3 Nanoparticle Synthesis	89
4.5.4 TEM Sample Preparation	90
4.5.5 pH Measurement.....	90
CHAPTER 5: CONCLUSIONS AND FUTURE DIRECTIONS	91
5.1 Conclusions	92
5.2 Future Directions.....	94
5.2.1 The Electron Donating Role of the Nanoparticle Precursor in the Synthesis of Gold Triangular Prisms	94
5.2.2 The Salt Dependence of DNA Hybridization on DNA Functionalized Nanoparticle Surfaces	96
5.2.3 The Mechanism of DNA Melting from DNA-Functionalized Nanoparticles	98

REFERENCES 100

LIST OF TABLES AND FIGURES

Figure 1.1. Scheme illustrating the synthesis of SNAs	17
Figure 1.2. Depiction of the library of SNAs	18
Figure 1.3. Cell-uptake studies comparing SNAs to linear DNA.....	19
Figure 1.4. Scheme illustrating the nanoflare design	25
Figure 1.5. Scheme illustrating the use of SNAs as programmable atom equivalents.....	26
Figure 2.1. Scheme illustrating hybridization of a DNA complement onto a spherical nucleic acid.....	32
Table 2.1. List of DNA sequences used for all experiments.....	35
Figure 2.2. Hybridization and dehybridization fluorescence curves	36
Figure 2.3. van 't Hoff plots and derived enthalpic gain and entropic cost.....	38
Table 2.2. Thermodynamic constants derived from the van 't Hoff analysis	38
Figure 2.4. Scheme illustrating isothermal titration calorimetry experiments	39
Figure 2.5. Isothermal titration calorimetry of hybridization of free DNA and on SNA.....	40
Table 2.3. Enthalpies obtained by direct integration of power (ΔP) vs. time peaks	41
Figure 2.6. ITC raw data of ligand dilution and a non-binding SNA.....	42
Figure 2.7. ITC of complement hybridization on SNAs with varying binding strand density	44
Figure 2.8. Schematic representation of course-grained MD simulations and calculated enthalpies of hybridization.....	45
Table 2.4. Break-down of energy contributions to the enthalpy of hybridization obtained from implicit-ion simulations.....	46

Table 2.5. Break-down of energy contributions to the enthalpy of hybridization obtained from explicit-ion simulations	46
Figure 2.9. Break-down of contributions to the difference in enthalpy of hybridization between an SNA and a linear DNA strand derived from implicit-ion coarse- grained MD simulations.....	47
Figure 2.10. Comparison of the structural energy obtained from implicit-ion simulations of the nanoparticle-attached DNA strand before and after hybridization	48
Figure 2.11. ITC data for linear DNA with and without T ₁₀ linker.....	49
Figure 2.12. ITC and enthalpy of hybridization onto SNAs for the first 4 complementary strands	51
Figure 2.13. Comparison of hybridization enthalpies obtained from implicit-ion simulations for SNAs functionalized with different DNA densities and linker lengths.....	51
Figure 2.14. Comparison of the total structural energy obtained from implicit-ion simulations of the remaining 45 unhybridized nanoparticle-bound DNA strands before and after hybridization of a complement.....	52
Figure 3.1. Scheme illustrating a DNA displacement reaction from a spherical nucleic acid	63
Figure 3.2. Scheme illustrating the ITC experiments to extract thermodynamic constants from displacement reactions	65
Table 3.1. Enthalpies of linear DNA displacement experiments	66
Figure 3.3. ITC plots of the hybridization experiment and the displacement experiment with linear DNA strands.....	67

	14
Figure 3.4. Enthalpy values for the hybridization and displacement from an SNA.....	68
Figure 3.5. ITC-derived enthalpy values for the hybridization and displacement from an SNA functionalized with T ₃₀ strands	69
Table 3.2. ITC derived enthalpy values for hybridization and displacement of different SNA constructs and linear DNA for comparison.....	69
Figure 3.6. ITC-derived enthalpy values for hybridization, displacement, and net reactions from SNAs as a function of nanoparticle diameter	70
Figure 4.1. Scheme illustrating the seed-mediated synthesis technique.....	74
Figure 4.2. Scheme illustrating how the nucleation pathway of gold triangular prisms can be probed.	76
Figure 4.3. Characterization of nanoparticles for use as precursors in prism growth	78
Figure 4.4. Gold nanoprism synthesis with large single-crystalline seeds.....	79
Figure 4.5. AFM analysis of prisms grown from large multiply-twinned gold nanoparticles	80
Figure 4.6. Gold nanoprism synthesis performed with CdSe@ZnS quantum dots.....	81
Figure 4.7. Representative image of the gold nanoprism and spherical impurity products	82
Figure 4.8. EDX analysis of prisms grown from palladium nanoparticle precursors.	83
Figure 4.9. Histogram of the size distribution.	83
Figure 4.10. Proposed mechanism for the alternate role of the nanoparticle precursors.....	84
Figure 4.11. Prism growth solutions with TiO ₂ nanoparticle precursors.....	86
Figure 4.12. Prism growth solutions with gold nanorods as precursors.....	87

Figure 5.1. Schematic of electron donating role of the nanoparticle precursor in the synthesis of gold triangular prisms	96
Figure 5.2. The salt dependence of the enthalpy, entropy and free energy of hybridization for free DNA and on an SNA.	97
Figure 5.3. Atomistic molecular dynamics simulations demonstrating the first 10ns of melting for a linear duplex and a nanoparticle-bound duplex.....	98

**CHAPTER 1: Introduction: Understanding the Structure-Function
Relationship of DNA-Nanoparticle Conjugates**

1.1 Summary

Spherical nucleic acids (SNAs) are conjugates composed of nanoparticle cores that are densely functionalized with radially oriented DNA. Compared to linear DNA, SNAs interact differently with biological systems. They readily enter cells, avert degradation by nucleases, and bind complementary DNA with 100-fold higher affinity constants than their linear counterparts. As a result of these properties, SNAs have been employed as gene regulation agents, medical diagnostic probes capable of detecting mRNA intracellularly, and as building blocks for programmable colloidal crystal assembly. The ability of SNAs to bind complementary DNA sequences with a higher affinity constant than linear DNA enables their application in all of these fields. Yet, little is known about the thermodynamic origin of binding on SNAs and how it changes with the SNA architecture, e.g. nanoparticle shape and DNA surface density.

A few fundamental questions that could help facilitate the implementation of anisotropic nanoparticle-DNA conjugates are addressed herein. The origin of enhanced binding on DNA-functionalized spherical particles is elucidated to extract the contributions from sterics and electrostatics that might be detrimental to the binding constant observed on more flat surfaces. The role of radius of curvature on the thermodynamics of displacement reactions is then examined to discern the effect of nanoparticle facet architecture on complex DNA reactions. Finally, the mechanism whereby different products form in low yielding syntheses of anisotropic nanoparticles is explored in order to inform how best to enhance the yield of desired products and move beyond a spherical nanoparticle architecture.

1.2 DNA Nanoparticle Conjugates: Their Properties and Applications

1.2.1 Introduction to Spherical Nucleic Acids

DNA-nanoparticle conjugates are constructs composed of nanoparticle cores (1-100nm in size) functionalized with short linear DNA strands. When the density of nanoparticle-bound DNA strands is high enough such that the DNA shell takes on the architecture of the underlying core, these conjugates are called spherical nucleic acids (SNAs) (Figure 1.1).^{1,2} This terminology highlights the spherical architecture of the DNA, which gives SNAs properties that are independent of nanoparticle core composition and are distinct from those of their linear counterparts.

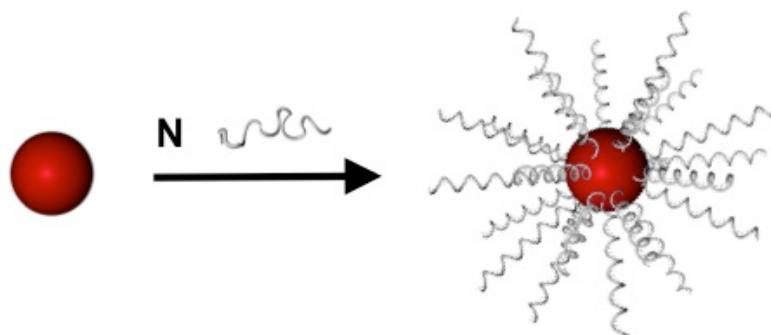


Figure 1.1. Scheme illustrating the synthesis of SNAs from their fundamental components, a nanoparticle core and short DNA oligomers

Despite SNA properties being derived primarily from the DNA architecture, substitution of the nanoparticle core can make SNAs more biodegradable, catalytically and optically active. Initially, SNAs were composed of citrate-capped gold nanoparticle cores and functionalized with alkylthiol-terminated DNA strands, relying on the strength of the gold-thiol covalent bond to favor functionalization.¹ A dense arrangement of DNA was achieved on a range of nanoparticle sizes with a salt aging step, which screens repulsive interactions between the negatively charged DNA backbones.^{3,4} This synthetic strategy has since been employed to create a library of SNAs

where the gold core can be substituted for a myriad of organic (i.e. liposomes and micelles), inorganic (i.e. silver and silica), and organic-inorganic composite (i.e. infinite coordination polymers and proteins) cores which impart SNAs with added functionality (Figure 1.2).⁵⁻¹⁵

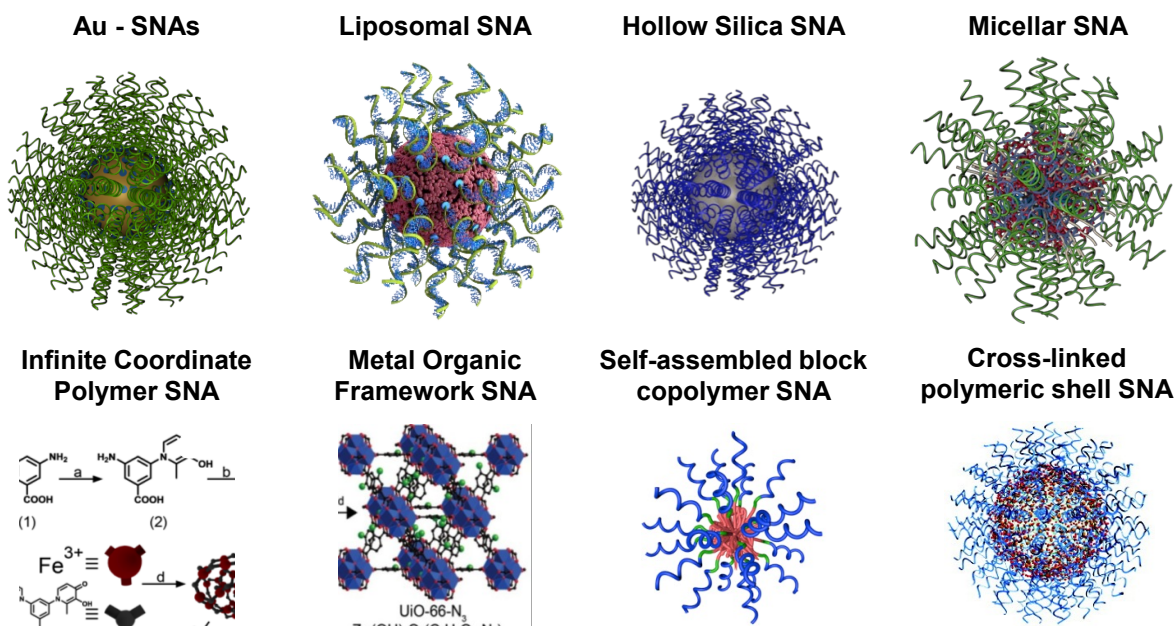


Figure 1.2. A library of SNAs representing the ability to tune the nanoparticle core independent of the DNA shell.

1.2.2 Core-Independent Properties of SNAs

The most striking and distinct properties of SNAs result from the dense arrangement of DNA that comprises the DNA shell. DNA confined to a spherical architecture around a nanoparticle core displays properties that are either not observed in linear DNA systems of identical sequence or enhanced relative to the linear counterparts.

1.2.2a Intracellular Delivery of Nucleic Acids

The ability to readily enter cells where linear DNA cannot is one of the most remarkable properties of SNAs.¹⁶ DNA is a negatively charged molecule that has difficulty penetrating the cell membrane's negatively charged phospholipid bilayer. Cellular uptake experiments using

epithelial cells demonstrate that dye-labeled linear DNA is not readily taken up by cells unless in the presence of a transfection agent, DharmaFECT (Figure 1.3 A,B). Conversely, SNAs of identical sequence are able to penetrate the cell membrane and readily deliver nucleic acids intracellularly (Figure 1.3C). Because transfection agents have been shown to be cytotoxic, SNAs present a significant technological advance for the intracellular delivery of nucleic acids.

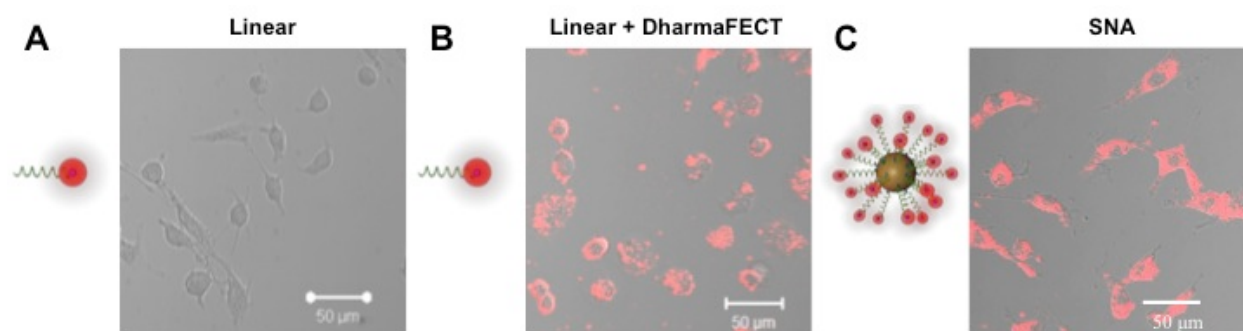


Figure 1.3. Epithelial cell uptake after 2 hours of exposure to fluorescently-labeled DNA in (A) linear form, (B) linear form plus a DharmaFECT transfection agent and (C) SNA form.

The marked difference in the ability of SNAs to enter cells where linear DNA cannot, is explained by their mechanism of cellular uptake.¹⁷ To determine that uptake of SNAs proceeds via a scavenger receptor mediated endocytosis mechanism a competitive assay was used. Four separate cell types were pretreated with fucoidan, a scavenger receptor ligand, and gold-nanoparticle SNA uptake was monitored by elemental analysis. In all cases, SNA content significantly decreased relative to untreated cells. Further, knockout cell lines confirmed that after engagement with scavenger receptor-A, uptake is specifically mediated by a caveolin-1 endocytotic pathway. This mechanism is in stark contrast to the method of passive diffusion linear DNA would take to enter cells, and is a direct result of the three-dimensional architecture of the SNA. DNA density,¹⁸ identity¹⁹ and sequence²⁰ are variables that can be tuned to modify the architecture of SNAs and affect cellular uptake. More densely packed SNAs of G-rich

sequences result in higher uptake. These findings emphasize that structural diversity in SNAs is what leads to marked differences in their interaction with biological systems, and provide a toolbox for synthesizing customized SNAs for a desired application.

1.2.2b Nuclease Resistance

Nucleic acids are prone to degradation by nucleases once inside cells, and exhibit significant losses in activity and functionality. SNAs have been shown to resist degradation by nucleases and are stable for longer than linear DNA of the same sequence.^{16,21} Such stability to degradation results again from the dense arrangement DNA around the nanoparticle core. Because DNA is negatively charged, cations associate with the backbone to decrease repulsive interactions with neighboring strands. This phenomenon increases the local cation concentration near the nanoparticle surface by up to an order of magnitude relative to the bulk concentration.²² Because nuclease activity decreases with increasing salt concentration, the high cationic environment afforded by the SNA architecture hinders nuclease efficacy and stabilizes the construct to degradation. Because this property is a result of the spherical DNA architecture, it can be modified with DNA density. Resistance to nuclease degradation by SNAs is proportional to DNA density and surface charge (i.e. higher density means higher charge and greater stability).²¹ These results are further confirmed by exposing SNA constructs of different densities to Turbo DNase, an enzyme whose activity is independent of salt concentration. SNAs of different densities exhibit similar degradation profiles upon exposure to Turbo DNase, in support of the high ionic charge hypothesis. The sum of these results again point to the DNA shell architecture as the primary contributor to the unusual properties of SNAs.

1.2.2c Enhanced Binding of Complementary DNA

One of the most interesting and enabling properties of SNAs is their ability to hybridize complementary DNA sequences with orders of magnitude higher binding constants than their linear counterparts.^{23,24} DNA hybridization is the process by which two complementary strands come together in solution to form a stable duplex. This process is exoergic and highly energetically favorable due to sequence specific hydrogen bonding and favorable van der Waals base stacking that drive duplex formation. Extensive experimental and theoretical studies have enabled the development of models that can reliably predict the energetics associated with DNA hybridization from the DNA sequence alone.²⁵⁻²⁷ These models have been used for the design of different SNA architectures, relying on the idea that if a DNA sequence behaves a certain way free in solution it will exhibit similar, if not identical, behavior when bound to a nanoparticle surface. This idea was tested by comparing the hybridization thermodynamics of a linear DNA 15mer to an SNA of the same sequence.²³ In this study, the SNA was treated as a single molecular entity and exposed to a stoichiometric amount of complement to mimic intracellular hybridization of nucleic acids present in small quantities. Temperature-dependent fluorescence hybridization studies yield thermodynamics constants from the concentration dependence of the DNA melting temperature. Strikingly, hybridization of complementary DNA to an SNA is energetically more favorable than hybridization to linear DNA with a binding constant that is two orders of magnitude larger. This enhanced binding can be attributed to the high DNA density around the particle, since the enhancement goes away when the nanoparticle size is increased but the DNA number is kept constant.

Additionally, binding on SNAs has been shown to be negatively cooperative.²⁴ The enhanced binding affinity observed on SNAs is only true for the first 10% of binding sites. Once

these sites are filled, it becomes enthalpically less favorable to hybridize to the SNA due to electrostatic and steric repulsion. Yet, as more strands hybridize, the entropic penalty to hybridization is partially alleviated on the SNA due to the preorganization of neighboring strands as more duplexes form. This trade-off between enthalpy and entropy can be manipulated by substituting a percentage of the DNA strands on the SNA for polyethylene glycol (PEG). This process has the effect of alleviating the electrostatic barrier to hybridization while taking advantage of the entropic gain on SNAs. Multiple binding events on PEG-DNA SNAs are therefore more favorable than on SNAs composed entirely of DNA.

1.2.3 Applications of SNAs

Because of these properties, specifically the enhanced binding to complementary DNA, SNAs can interact with nucleic acids in biological contexts very differently than their linear counterparts. This has led to the use of SNAs as the basis for a variety of different technological innovations.

1.2.3a Gene Regulation Agents

Gene expression is the fundamental way by which an organism's genetic information, DNA, is converted to functional gene products such as RNA and protein. These gene products then go on to carry out all cellular function and give organisms their phenotype. When organisms respond to environmental stressors, they experience changes in gene expression. Because these changes often manifest as disease states, regulation of gene expression is a central goal in the development of nucleic acid-based therapeutic agents.

SNAs are ideal candidates as therapeutic agents for gene regulation through short interfering RNA (siRNA) or antisense DNA, because they can enter cells readily, avert degradation and bind complements at exceptionally low concentrations. Many disease states are

associated with the upregulation of mRNA, which manifests as an overexpression of translated protein. Nucleic acid identity and sequence can be readily tuned on the SNA to be complementary to an upregulated mRNA and inhibit the protein translation pathway. Therefore, the SNA design can fit the specific therapeutic application. The down-regulation of green fluorescent protein (GFP) with antisense SNAs in cells was the first demonstration of SNAs as viable intracellular regulatory agents.¹⁶ Since this first demonstration, SNAs have been implicated as therapeutic agents in a variety of diseases. They can penetrate the skin to treat inflammatory skin disorders²⁸ and promote wound healing in diabetic mice.²⁹ Importantly, SNAs can penetrate the blood-brain barrier, and have been shown to significantly improve mice survival in the treatment of glioblastoma, an aggressive form of brain cancer.³⁰

1.2.3b Intracellular mRNA Detection Probes

For the study of gene expression, methods for detection of RNA have been critical. Because RNA is transcribed from DNA, it is a direct measure of an organism's response to its environment. RNA serves many roles in the cell including protein translation, sensing, regulation of gene expression, and catalysis.³¹ As such, uncontrolled RNA expression is a first indicator of cellular stress.

Detection of relative levels of all RNA within a cell, termed the transcriptome, is important for whole genome sequencing applications. There are two common ways to measure RNA in a multiplex manner on a population of cells, DNA microarrays and real-time reverse transcription polymerase chain reaction (RT-qPCR). DNA microarrays consist of a large number of single stranded DNA of pre-defined sequences, packed onto a surface in a dense arrangement, and used to capture RNA from a cell lysate.^{32,33} This technique relies on the ability of RNA to hybridize surface bound strands, solid-phase hybridization, and release a signal, usually fluorescence.³⁴

RT-qPCR is a three-step process by which RNA from a lysate is converted to complementary DNA (cDNA) by the enzyme reverse transcriptase, cDNA is amplified by PCR and detected in real time for quantification. Both microarray and RT-qPCR methods have greatly improved our understanding of how gene expression levels change over cell populations, but have limited sensitivity for detecting cell-to-cell gene expression variability and are fundamentally incompatible with live cell imaging, as these techniques require cell lysis. Additionally, obtaining information about intracellular localization of RNA, which is important for understanding dynamic processes like cell division, can be challenging.³⁵ These techniques require fractionation and accumulation of intracellular components in fixed cells at specific times. Thus multiplex techniques provide a global and static representation of gene expression across cell populations.

A dynamic perspective of how RNA is localized inside cells comes from *in situ* hybridization studies with tools like molecular beacons.^{36,37} *In situ* hybridization is a technique that employs nucleic acid probes to hybridize and identify RNA and DNA targets inside tissues and is therefore used to localize specific sequences within an organism. Molecular beacons are a type of single-stranded DNA probe with a stem-loop structure and great sensitivity for distinguishing single nucleotide mismatches in targets. The DNA probe is labeled with a fluorophore at one end and a quencher at the other. In the absence of target, the DNA assumes a loop structure based on Watson-Crick intramolecular base pairing and the fluorophore is quenched. An RNA target of interest will bind the single-stranded loop region of the beacon, break up the pre-formed duplex and trigger fluorescence turn-on. *In situ* hybridization of live cells, either with molecular beacons or other probes, has provided insight into the dynamic complexity and cell-to-cell variability of gene expression.³⁸ However, these methods are limited

by the ability to deliver the molecular probes to the cell. Because they are negatively charged, nucleic acids do not inherently enter cells. Intracellular delivery of molecular probes requires a transfection agent, usually a liposome, which makes them inherently immunogenic and toxic and limits the concentrations in which the probes can be delivered

A construct that has been employed to address many of these challenges in intracellular oligonucleotide detection is the nanoflare (Figure 1.4).³⁹⁻⁴¹ The nanoflare is a construct consisting of an SNA base. Fluorophore-labeled complementary strands (“flares”) are hybridized to the particle-bound DNA, such that fluorescence of the flare is quenched when in close proximity with the metallic nanoparticle.⁴²

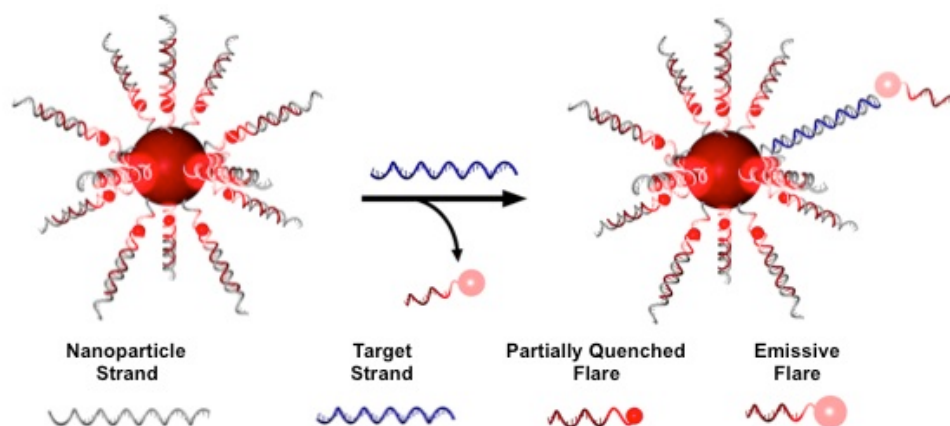


Figure 1.4. Scheme illustrating the nanoflare design where a target strand displaces a nanoparticle-bound short flare strand to turn on fluorescence.

For RNA detection with the nanoflare, the target RNA must have a sequence that has a greater degree of complementarity to the particle-bound DNA strand. Target hybridization forces the short flare to be released resulting in fluorescence turn-on. DNA surface sequence modification has enabled the development of multiplexed nanoflares capable of detecting more than one mRNA sequence at a time.³⁹ The high DNA density on the nanoflare surface makes it

resistant to nuclease degradation once inside the cell and gives it a higher affinity constant than linear DNA. A higher affinity constant translates to orders of magnitude more sensitivity in the detection of RNA with nanoflares, which is crucial when targeting disease markers present at low concentrations.

1.2.3c Building Blocks for Colloidal Crystallization

The use of SNAs as programmable atom equivalents (PAEs) has enabled the construction of hierarchically ordered colloidal crystals from the bottom up.^{1,43–47} This view of the PAE building block takes inspiration from Pauling’s rules for atomic crystallization of ionic solids and treats the nanoparticle as an “atom” that imparts directionality to the DNA “bond” (Figure 1.5A). The weak, polyvalent and cooperative binding interactions of the DNA shell can be programmed for the assembly of PAEs into well-defined crystal lattices (Figure 1.5B), relying on classic crystallization slow cooling and annealing methods to achieve the thermodynamically favored crystal habit (Figure 1.5C).⁴⁸

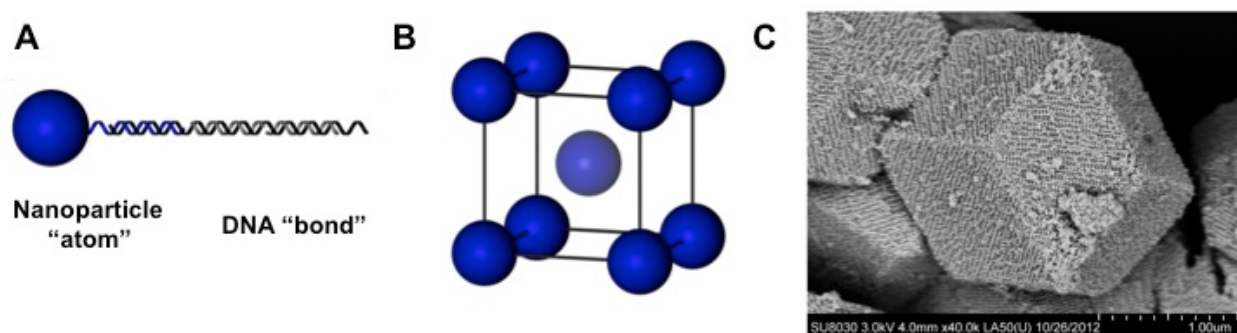


Figure 1.5. Depiction of SNAs as programmable atom equivalents (PAEs). (A) PAE architecture where the nanoparticle acts as an atom and the DNA as a bond. (B) DNA interactions can be used to assemble PAEs into pre-determined unit cells which form (C) micron-sized crystals in the thermodynamically favorable crystal habit.

Thermodynamically controlled assembly of PAEs into superlattices with long range ordering relies on the principle that PAEs will assemble to maximize the number of DNA interactions for a given nanoparticle size, DNA sequence, length and flexibility. This principle has been tested, and the programmable assembly of dozens of superlattice symmetries has been predicted and achieved experimentally, leading to the establishment of a set of design rules for binary and ternary systems.^{45,46,49}

Unlike in atomic systems, the nanoparticle core identity of PAEs (i.e. chemical and physical properties) is independent of the identity of the DNA shell. This means that superlattices of different chemical compositions can be synthesized with identical structural parameters.⁵⁰ The programmability of the DNA also allows for interparticle spacing to be tuned with sub-nanometer precision.⁵¹ The ability to then transfer these superlattices to the solid state by encapsulating them in silica,⁵² has enabled both the characterization of these systems with microscopy techniques and expanded their potential use in a variety of applications such as optics, photonics and electronics.^{53–55}

The programmable assembly of SNAs relies heavily on their binding properties, which can direct crystallization down a thermodynamic path or, if improperly designed, fall into kinetic traps. Accurate prediction of the DNA bond strength depends on understanding what factors determine duplex formation on SNAs, and can facilitate the synthesis of hierarchical materials in a predictable manner.

1.3 Introduction to Thesis Topics: Understanding the Effect of SNA Architecture on

Binding

The use of SNAs in all of their applications depends fundamentally on the binding of complementary DNA. Yet, little is known about the thermodynamic origin of this process and

how it changes with SNA architecture. In order to move beyond the spherical architecture of the SNA to implement more biologically relevant and optically interesting anisotropic cores, the effect of SNA architecture on the ability to bind complementary DNA must first be understood. Hereafter, three fundamental questions about the SNA architecture and how it affects binding are addressed.

1.3.1 Explaining the Origin of Enhanced Binding on SNAs

One of the most applicable and also intriguing properties of SNAs is their ability to bind DNA with a binding constant that is orders of magnitude larger than that of linear DNA. There are several parameters that vary greatly between hybridization to an SNA and hybridization to linear DNA, but the microarray literature acknowledges unfavorable electrostatics as the largest contributor preventing the insertion of a linear strand into the dense array of surface-bound DNA strands.⁵⁶⁻⁶⁰ Previous work with DNA-functionalized, spherical, gold nanoparticles has demonstrated that by decreasing nanoparticle size, researchers were able to more densely functionalize particle surfaces with DNA.^{3,4} The implication of this work is that as the nanoparticle radius increases, the DNA is less splayed and electrostatic repulsion between DNA's negatively charged phosphate backbones is maximized. This radius of curvature dependence of the electrostatics could have negative repercussions on the binding constant of anisotropic DNA-nanoparticle conjugates, because anisotropic particles are primarily bound by flat facets. With these considerations, an understanding of the origin of binding enhancement observed on SNAs would help tease out the contributions from electrostatics on the binding constant, and inform the thermodynamic design considerations for anisotropic DNA-nanoparticle conjugates.

1.3.2 The Role of Radius of Curvature on DNA Displacement Reactions on SNAs

Despite the indisputable evidence regarding radius of curvature's effects on DNA loading on nanoparticles, it is not self-evident that radius of curvature will have the same effect on surface hybridization let alone the types of displacement reactions that enable the design of intracellular mRNA probes or nanoflares. A study on the effect of surface density and radius of curvature on the thermodynamics of DNA displacement reactions will directly mimic the nanoflare design. This study will inform the design considerations for successful displacement reactions on surfaces.

1.3.3 Elucidating the Mechanism of Gold Nanoprism Formation to Improve Reaction Yield

Gold triangular nanoprisms are anisotropic particles synthesized by seed-mediated synthesis. This synthesis, like many other syntheses of low symmetry nanoparticles, yields a broad product distribution. Though purification techniques have been developed to achieve prisms in greater than 95% yields,^{61,62} this limitation challenges the role of the nanoparticle precursor as a seed and suggests the possibility of an alternate nucleation pathway. A method to probe the role of the nanoparticle precursor in gold triangular prism nucleation is presented. Compositional and structural "labels" are employed to track the final fate of the seed among synthesis products with the final goal of proposing a mechanism by which prism nucleation and growth proceeds. A mechanistic understanding of the nucleation and growth of triangular prisms will enable the informed optimization of product yield and facilitate the implementation of prisms in the design of anisotropic nanoparticle-DNA conjugates.

**CHAPTER 2: The Role of Structural Enthalpy in Spherical Nucleic Acid
Hybridization**

Portions of this chapter are adapted from *J. Am. Chem. Soc.* **2018** DOI: 10.1021/jacs.8b03459

Collaborators: Ziwei Wang, George Schatz, Erik Luijten and Chad Mirkin

2.1 Summary

DNA hybridization onto DNA-functionalized nanoparticle surfaces (e.g., in the form of a spherical nucleic acid (SNA)) is known to be enhanced relative to hybridization free in solution. Surprisingly, via isothermal titration calorimetry we reveal that this enhancement is enthalpically, as opposed to entropically, dominated by ~ 20 kcal/mol (Figure 2.1). Coarse-grained molecular dynamics simulations suggest that the observed enthalpic enhancement results from structurally confining the DNA on the nanoparticle surface and preventing it from adopting enthalpically unfavorable conformations like those observed in the solution case. The idea that structural confinement leads to the formation of energetically more stable duplexes is evaluated by decreasing the degree of confinement a duplex experiences on the nanoparticle surface. Both experiment and modeling confirm that when the surface-bound duplex is less confined, i.e., at lower DNA surface density or at greater distance from the nanoparticle surface, its enthalpy of formation approaches the less favorable enthalpy of duplex formation for the linear strand in solution. This work provides insight into one of the most important and enabling properties of SNAs, and will inform the design of materials that rely on the thermodynamics of hybridization onto DNA-functionalized surfaces, including diagnostic probes and therapeutic agents.

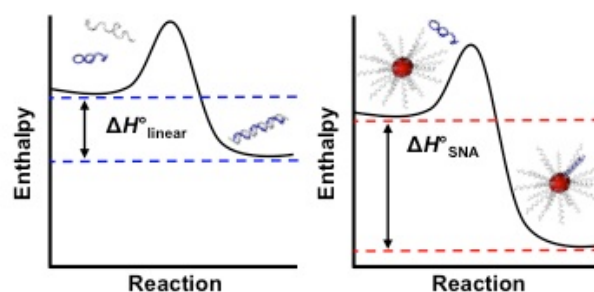


Figure 2.1. Scheme illustrating that hybridization of a DNA complement onto a spherical nucleic acid is enthalpically enhanced relative to linear DNA hybridization.

2.2 Introduction

Spherical nucleic acids (SNAs) are a class of structures typically made by arranging linear nucleic acids at high density around a nanoparticle core.^{1,2} SNAs have become important entities in the development of medical diagnostic probes,^{63,64} intracellular small-molecule detection agents, RNA tracking agents,^{39–41,65} and building blocks for colloidal crystal engineering.^{44,45,66–69} Their unique properties, which are highly differentiated from linear structures, make them very attractive for such uses. One of these properties is a higher affinity constant for complementary nucleic acids. Depending on sequence, SNAs can bind complements orders of magnitude more tightly than linear forms of the same sequence.^{23,24,70} Despite the importance of this enhanced binding for many of the SNA applications, its origin remains unknown.

Given the restricted nature and pre-orientation of the short strands that define SNAs, enhancement of hybridization could be attributed to entropic contributions. In the process of nanoparticle functionalization with DNA, strands lose degrees of freedom as the surface environment becomes increasingly more crowded. It is therefore conceivable that by conformationally restricting one of the DNA strands to a nanoparticle surface on the SNA, part of the entropic cost is paid prior to hybridization. For linear DNA, the entropic cost is paid in full during hybridization. Consequently, hybridization on the SNA should be entropically enhanced.

However, complement binding on SNAs carries a *higher* entropic penalty than binding in the linear form.²³ Here, we use temperature-dependent fluorescence melting studies, isothermal titration calorimetry (ITC), and coarse-grained molecular dynamics (MD) simulations to determine the entropy and enthalpy of hybridization for linear DNA binding as well as binding of a complement to an SNA. We demonstrate that the binding enhancement on SNAs is instead

enthalpically driven and via a combination of experiment and modeling explain its thermodynamic origin.

2.3 Results and Discussion

2.3.1 Binding Enhancement Onto SNAs is Confirmed by Concentration-Dependent

Fluorescence Hybridization Experiments.

To determine the entropies and enthalpies of binding, we performed concentration-dependent fluorescence hybridization experiments.²⁵ We studied, under identical conditions, a linear 12-mer DNA system and 5.9 nm gold nanoparticle SNAs functionalized with ~46 DNA strands of the same sequence (Table 2.1). Complementary strands were labeled with a fluorophore, which served as a reporter for hybridization. Linear strands were labeled with a molecular quencher while the gold core on the SNAs served as a plasmonic quencher. At high temperatures, when strands are unhybridized, fluorescence is highest. When the temperature is decreased, hybridization forces the fluorophore into proximity with the quencher and a hybridization transition can be observed (Figure 2.2 A,B). Both systems were prepared in a 1:1 stoichiometry of either SNA or linear DNA to complementary strand, and a DNA helix-coil transition temperature was measured over a range of concentrations (Figure 2.2 C,D).

Table 2.1. List of DNA sequences used for all experiments.

#	LABEL	SEQUENCE
1	12-mer Linear	5' TCCAATCATACT 3'
2	12-mer Linear Dabcyl quencher	5' [DABCYL]TCCAATCATACT 3'
3	Complementary 12-mer	5' AGTATGAGTGGA 3'
4	Complementary 12-mer Dye	5' AGTATGAGTGGA [AF488] 3'
5	SNA_T ₁₀ 12-mer	5' TCCAATCATACT(T ₁₀)-propylthiol-3'
6	SNA_T ₃₀ 12-mer	5'-TCCAATCATACT(T ₃₀)-propylthiol-3'
7	SNA_T ₂₂	5' TTTT TTTT-propylthiol-3'
8	12-mer Linear T ₁₀	5' TCCAATCATACT(T ₁₀) 3'

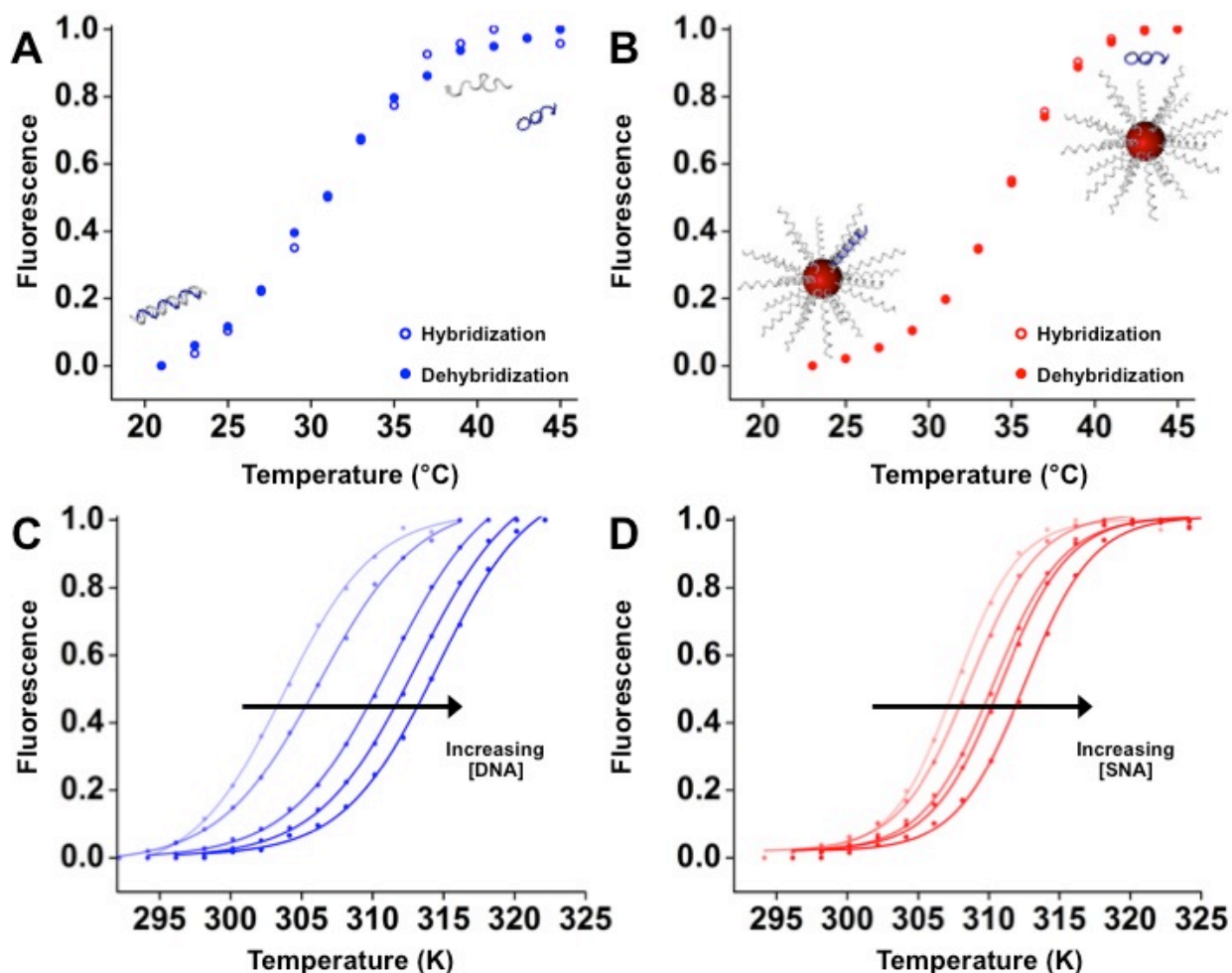


Figure 2.2. Hybridization and dehybridization fluorescence curves at the lowest sample concentrations (1 nM complementary DNA) for (A) 1 nM linear DNA and (B) 1 nM SNAs. Concentration dependence of the helix–coil transition temperature for (C) linear DNA hybridization and (D) SNA hybridization.

The concentration dependence of the helix–coil transition temperature reflects the thermodynamics of hybridization through the van 't Hoff relationship^{26,71}

$$\frac{1}{T_m} = \frac{R}{\Delta H^\circ} \ln C_T + \frac{\Delta S^\circ - R \ln 4}{\Delta H^\circ},$$

where T_m is the transition temperature, C_T the combined concentration of SNA (or linear DNA) and complement, R the gas constant, and ΔH° and ΔS° are the enthalpy and entropy of

hybridization, respectively. The absence of hysteresis between hybridization and dehybridization curves at the lowest sample concentrations reflects measurements being made under thermodynamic equilibrium (Figure 2.2 A,B).

Thermodynamic constants are derived from linear regression of these temperature versus concentration data (Figure 2.3, Table 2.2). The less steep slope for the SNA system reveals that the binding enthalpy on SNAs, $\Delta H^\circ = -91.3 \pm 5.5$ kcal/mol, is far more favorable than for linear DNA, $\Delta H^\circ = -40.6 \pm 2.4$ kcal/mol (Figure 2.3). Remarkably, the SNA system also exhibits a higher entropic loss upon hybridization, with $T\Delta S^\circ = -75.8 \pm 5.3$ kcal/mol at 298 K vs. $T\Delta S^\circ = -27.2 \pm 2.3$ kcal/mol for linear DNA. Since the increased enthalpic gain in the SNA system more than compensates the larger entropic cost, the free energy of hybridization is lower for SNAs than for linear DNA ($\Delta G^\circ_{\text{SNA}} = -15.5 \pm 0.2$ kcal/mol vs. $\Delta G^\circ_{\text{linear}} = -13.4 \pm 0.1$ kcal/mol), and the association constant is correspondingly higher, $K_{\text{eq}}^{\text{SNA}} = (2.3 \pm 0.8) \times 10^{11} \text{ M}^{-1}$ vs. $K_{\text{eq}}^{\text{linear}} = (6.8 \pm 1.1) \times 10^9 \text{ M}^{-1}$. Whereas the enhanced binding confirms prior observations,^{23,24,70} the larger entropic penalty for SNA binding and the increased enthalpic gain are puzzling given the conformational constraints of the nanoparticle bound DNA and the view that the dense packing of DNA on the SNA is likely to result in destabilizing steric and electrostatic interactions.⁵⁶⁻⁶⁰ Indeed, we have observed such thermodynamic trends before²³ but refrained from commenting on their origin because of lack of a suitable explanation.

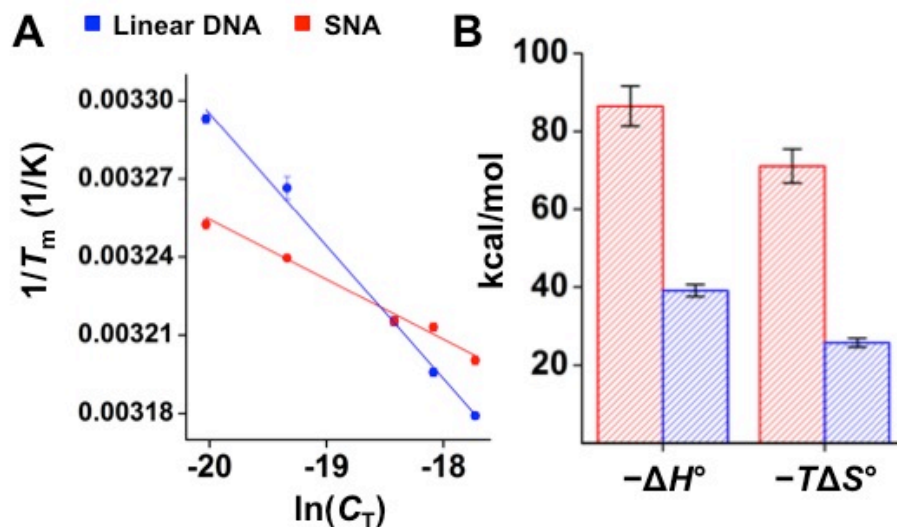


Figure 2.3. (A) van 't Hoff plots from which thermodynamic constants are extracted for binding between a complementary linear strand and either linear 12-mer DNA (blue) or SNAs (red). (B) Comparison of enthalpic gain and entropic cost derived from the van 't Hoff plots.

Table 2.2. Thermodynamic constants derived from the van 't Hoff analysis.

Thermodynamic Constant	Linear DNA	SNA
ΔH° (kcal/mol)	-40.6 ± 2.4	-91.3 ± 5.5
$T\Delta S^\circ$ (kcal/mol)	-27.2 ± 2.3	-75.8 ± 5.3
ΔG° (kcal/mol) at 298 K	-13.4 ± 0.1	-15.5 ± 0.2
K_{eq} (M^{-1}) at 298K	$6.8 \times 10^9 \pm 1.1 \times 10^9$	$2.3 \times 10^{11} \pm 8.5 \times 10^{10}$

2.3.2 Isothermal Titration Calorimetry Confirms that Hybridization Enthalpy on SNAs is More Favorable Than in the Linear Case

The van 't Hoff analysis assumes that DNA hybridization proceeds in a two-state manner and that the enthalpy of this process is temperature-independent.²⁶ Since these assumptions have been shown to significantly affect van 't Hoff-derived enthalpies of linear DNA hybridization,^{72–74} we sought to corroborate our findings with a model-independent technique. Specifically, to confirm the larger enthalpy of hybridization for SNAs, we performed ITC experiments on the

with inflection points at molar ratios of 4 and 15 strands per particle (Figure 2.5B). This shape implies that SNAs exhibit a type of negative cooperativity, where binding of the first 4 strands is enthalpically more favorable than subsequent hybridization events. Such negative cooperativity is consistent with prior observations.²⁴

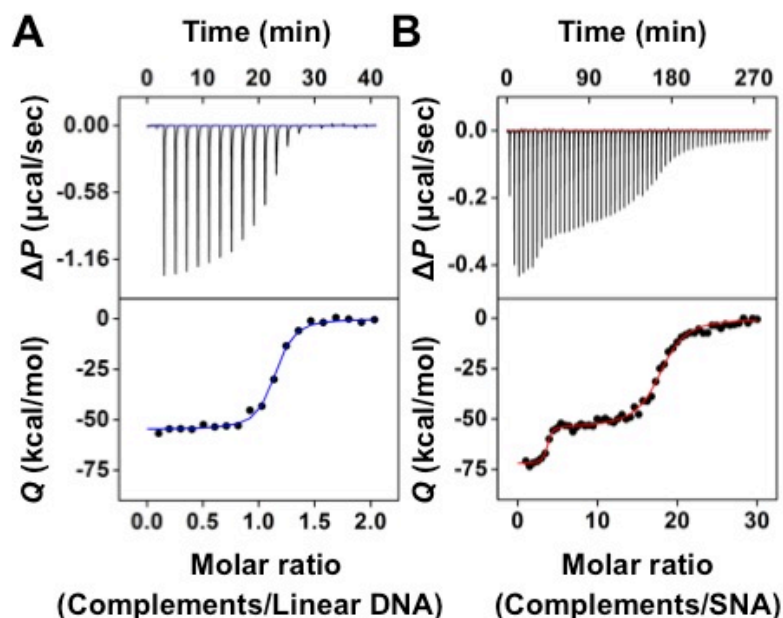


Figure 2.5. Isothermal titration calorimetry of (A) 12-mer DNA duplex hybridization free in solution and (B) 12-mer DNA duplex hybridization on SNAs functionalized with ~46 strands per particle. (Upper panel: differential heating power ΔP vs. time, lower panel: integrated heats of reaction Q vs. molar ratio.)

The ITC curves also directly yield the hybridization enthalpies from the released heat Q , showing an enthalpy gain that is 20.7 ± 2.2 kcal/mol higher for binding on SNAs (Table 2.3). To ensure that the enthalpic difference between the SNA and linear systems was strictly the result of differences in the strength of duplex formation in the two systems, control experiments were performed to rule out other enthalpic contributions (Figure 2.6-2.8). The heat of complementary DNA dilution was determined by titrating complementary DNA into a buffer solution composed

of water at 0.01% sodium dodecyl sulfate, and 0.3 M sodium chloride (Figure 2.6A). Additionally, to measure the heat of nonspecific association of complementary DNA with the SNAs, complementary DNA strands were titrated into a solution of SNAs functionalized with 45 non-complementary, polythymine DNA strands (Figure 2.6B). Neither complementary DNA dilution nor non-specific association with SNAs contributes significantly to the difference in hybridization enthalpies observed between the SNA and linear systems. We therefore conclude that hybridization onto SNAs is enthalpically enhanced relative to linear DNA hybridization.

Table 2.3. ITC-derived enthalpies obtained by direct integration of power (ΔP) vs. time peaks. For further analysis, the ITC data was fitted to either a one-site binding model (in the case of linear DNA) or a two-site binding model (in the case of SNAs). A two-site binding model for SNAs was based purely on the shape of the calorimetrically derived isotherm, which has two inflection points. This type of fitting allowed extraction of model-dependent thermodynamic constants (ΔS° , K_{eq}). Data for both types of binding sites on the SNA are listed consecutively when applicable. SNA sample names are listed based on the sequence of DNA used (see the methods section for a list of sequences). Labels “High” and “Low” refer to high and low density of DNA on the nanoparticles, respectively.

Sample	Loading	<i>N</i> (Stoichiometry)	ΔH° (kcal/mol)	ΔS° (kcal/mol *K)	K_{eq} (M ⁻¹)
SNA_T ₁₀ 12-mer (High)	46 ± 1	4	-74.5 ± 2.1	-0.207 ± 0.009	2.58×10 ⁹ ± 2.73×10 ⁹
		15	-54.5 ± 1.5	-0.152 ± 0.005	6.03×10 ⁶ ± 1.79×10 ⁶
SNA_T ₁₀ 12-mer (Low)	30 ± 1	3	-68.1 ± 1.7	-0.181 ± 0.005	2.39×10 ⁹ ± 6.94×10 ⁹
		4	-57.9 ± 3.5	-0.164 ± 0.006	6.82×10 ⁶ ± 9.09×10 ⁵
SNA_T ₃₀ 12-mer	45 ± 1	3	-58.5 ± 1.9	-0.152 ± 0.008	5.05×10 ⁸ ± 4.68×10 ⁸
		14	-53.0 ± 4.7	-0.147 ± 0.016	5.08×10 ⁶ ± 1.34×10 ⁶
SNA_T ₂₂	51 ± 1	N/A	-4.6 ± 1.6	N/A	N/A

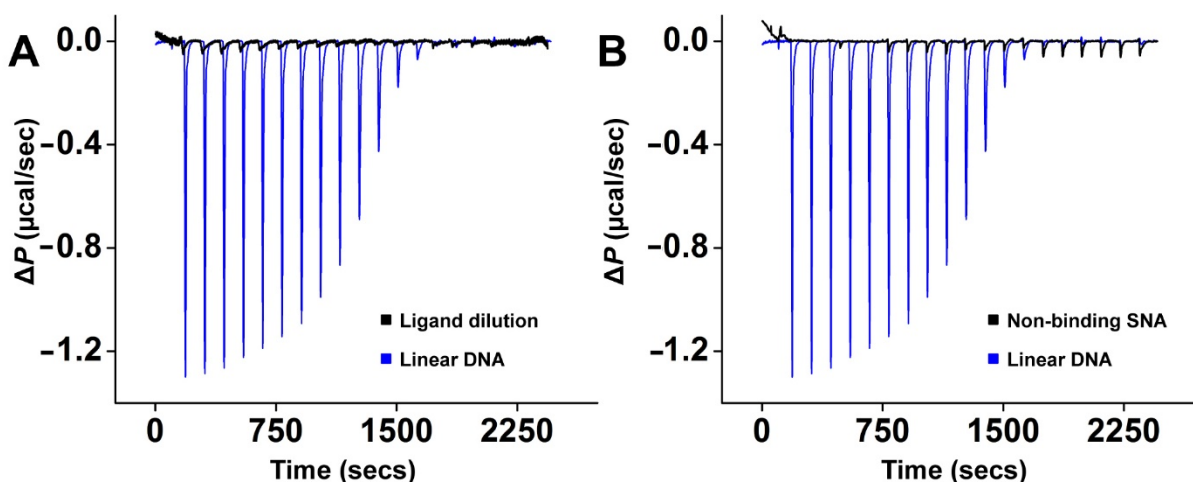


Figure 2.6. Shown in black are (A) the heat of complementary DNA dilution, determined by titrating complementary DNA into buffer (0.01% SDS, 0.3 M NaCl) and (B) the heat of complementary DNA association with a non-binding SNA, determined by titrating complementary DNA into a solution containing SNAs functionalized with 45 non-complementary DNA strands (polyT). Raw power data for linear DNA hybridization is provided in blue for comparison in each case.

SNA_T ₁₀ 12-merT ₂₂ _5050	53 ± 1	3	-75.1 ± 1.5	-0.229 ± 0.005	2.24 × 10 ⁸ ± 1.15 × 10 ⁸
SNA_T ₁₀ 12-merT ₂₂ _2525	48 ± 1	3	-74.3 ± 3.4	N/A	N/A
Linear 12-mer	N/A	1	-53.8 ± 0.8	-0.147 ± 0.003	2.05 × 10 ⁷ ± 5.62 × 10 ⁶
Linear 12-mer T ₁₀	N/A	1	-56.4 ± 0.6	-0.155 ± 0.004	1.94 × 10 ⁷ ± 3.03 × 10 ⁶

The agreement between these data and the fluorescence data suggests that the relative entropic and enthalpic contributions determined from the van 't Hoff analysis are qualitatively reliable, despite the assumptions of the model. Discrepancies in the absolute values of hybridization enthalpies derived from calorimetry and from the van 't Hoff analysis have been previously observed in linear DNA systems.^{77,78} The differences can be explained by deviations from two-state behavior²⁶ and by changes in heat capacity associated with DNA melting.^{72-74,78}

We suspect that both effects play a role in the systems under study, and if considered in the van 't Hoff analysis may lead to better agreement with calorimetric values.

With strong evidence to support that binding to the SNA is enthalpically more favorable than binding in linear DNA, we next sought to explain the origin of this enhancement. The high density of binding sites on the SNA architecture has been shown to result in cooperative binding in colloidal crystallization experiments.⁷⁹ To examine if the enthalpic enhancement observed on SNAs was a result of nearest-neighbor cooperative binding, the number of binding sites on the nanoparticle surface was decreased while maintaining the same density of DNA strands (~45 strands/particle). This was achieved by introducing a non-binding filler strand of the same length, polythymine T₂₂. SNAs were functionalized with either 25:75 binding to non-binding DNA (Figure 2.7A) or 50:50 binding to non-binding DNA (Figure 2.7B). Hybridization enthalpy of the first few binding events was plotted as a function of percentage of binding strands on the SNA. The original SNA has 100% binding strands, while a control non-binding SNA has 0% binding strands (Figure 2.7C). Interestingly, these experiments show that the enthalpy of hybridization for the first few strands on SNAs does not depend on the ability of neighboring single strands to form productive duplexes. An enhancement in the hybridization enthalpy on SNAs relative to linear DNA is solely a consequence of the surface density of DNA.

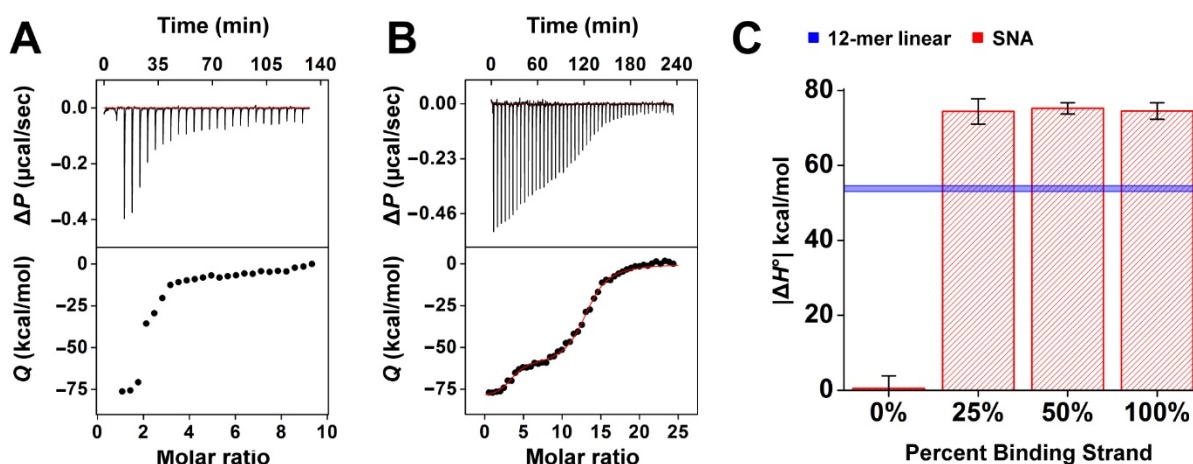


Figure 2.7. ITC of complement hybridization on SNAs functionalized with (A) 25:75 binding to non-binding DNA and (B) 50:50 binding to non-binding DNA. C) Hybridization enthalpy of the first few binding events plotted as a function of percentage of binding strands on the SNA. The enthalpies of a completely binding SNA (100%) and a completely non-binding SNA (0%), as well as the enthalpy of linear strand hybridization (blue) are provided for reference. (A,B): Upper panels: differential heating power ΔP vs. time; lower panels: integrated heats of reaction Q vs. molar ratio.

2.3.3 Coarse-Grained Molecular Dynamics Simulations Demonstrate that the Enthalpic

Binding Enhancement Observed on SNAs Results From Structural Confinement of the DNA

To understand the role of DNA density on the enthalpy of complement hybridization onto SNAs we turned to coarse-grained MD simulations. Simulations of the hybridized and the unhybridized state were performed for both the linear and the SNA systems using the 3SPN.2 model.^{80–82} This model separates the DNA into three sites per nucleotide, one each for the phosphate, sugar, and base, and has been parametrized to reproduce correct structural, thermodynamic, mechanical, and kinetic properties of DNA. Assuming incompressibility, we computed the enthalpy of duplex formation as⁸³

$$\Delta H^\circ \approx E_H - (E_U + E_S) ,$$

where E_H is the internal energy of the system with a hybridized duplex, E_U the internal energy of the unhybridized strands, and E_S the energy of a single complementary DNA strand in solution (Figure 2.8A). The simulations confirmed the experimentally observed trend for the enthalpy of hybridization, with an enhancement of ~ 5.3 kcal/mol associated with hybridization on the SNA relative to free in solution (Figure 2.8B, Table 2.4). To achieve high statistical accuracy, the simulations were performed with implicit ions, using the Debye–Hückel approximation, but we confirmed that the same trends are obtained when using explicit salt and counterions (Table 2.5).

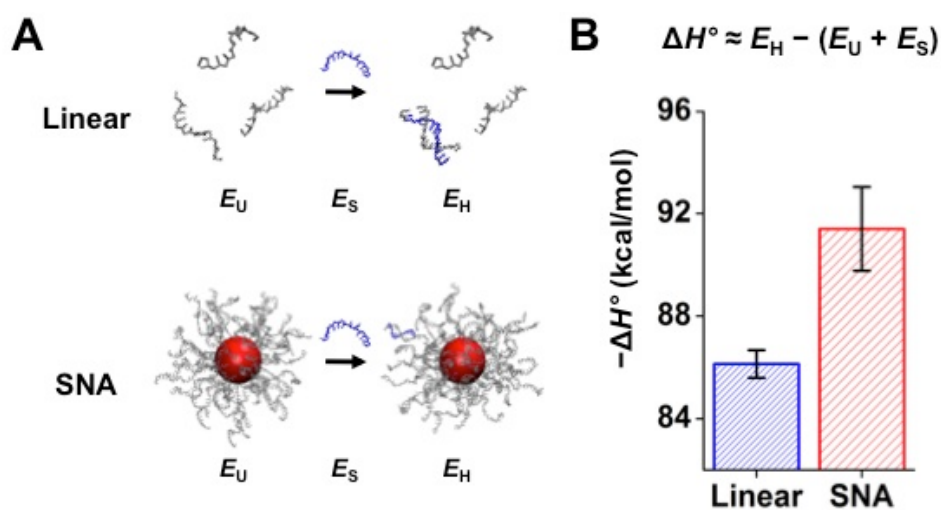


Figure 2.8. (A) Coarse-grained MD simulations of 12-mer DNA before (E_U) and after (E_H) duplex formation free in solution and on an SNA functionalized with 46 strands. (B) Comparison of simulation-derived enthalpies of hybridization for a duplex formed free in solution and one formed on an SNA.

Table 2.4. Break-down of energy contributions to the enthalpy of hybridization obtained from implicit-ion simulations.

Sample	ΔH (kcal/mol)	ΔE (Structural)	ΔE (BP)	ΔE (CS)	ΔE (Coulomb)	Δn_{bp}
Linear	-86.13 ± 0.54	-34.04 ± 0.62	-44.03 ± 0.04	-8.76 ± 0.01	0.48 ± 0.01	8.97 ± 0.09
SNA	-91.41 ± 1.64	-38.37 ± 1.70	-44.78 ± 0.07	-9.07 ± 0.02	0.81 ± 0.10	9.14 ± 0.14

Table 2.5. Break-down of energy contributions to the enthalpy of hybridization obtained from explicit-ion simulations.

Sample	ΔH (kcal/mol)	ΔE (Structural)	ΔE (BP)	ΔE (CS)	ΔE (Coulomb)	Δn_{bp}
Linear	-79.40 ± 1.03	-55.86 ± 0.34	-45.27 ± 0.02	-8.96 ± 0.01	-9.89 ± 0.37	9.35 ± 0.01
SNA	-84.70 ± 1.34	-60.37 ± 1.81	-45.85 ± 0.05	-9.25 ± 0.01	-9.81 ± 0.44	9.50 ± 0.01

Owing to the lack of explicit solvent, ΔH° differs quantitatively from the experimental values. However, the simulations make it possible to separate the inter- and intra-molecular contributions. To identify the primary origin of the observed enthalpic enhancement, we broke down the hybridization enthalpies of the linear duplex and the SNA duplex into (i) inter-strand base-pairing, (ii) cross-stacking, (iii) electrostatic, and (iv) intra-strand structural energies (Figure 3.9, Tables 3.4-3.5). For each of these contributions, we defined $\Delta\Delta H$ as the difference between the enthalpy of hybridization on the SNA (ΔH_{SNA}) and the enthalpy of hybridization for linear DNA (ΔH_{linear}). We found that the main contribution to the enhancement of ΔH° on the SNA is the change in structural energy, which comprises covalent-bond, angle, dihedral, and base-stacking energies.

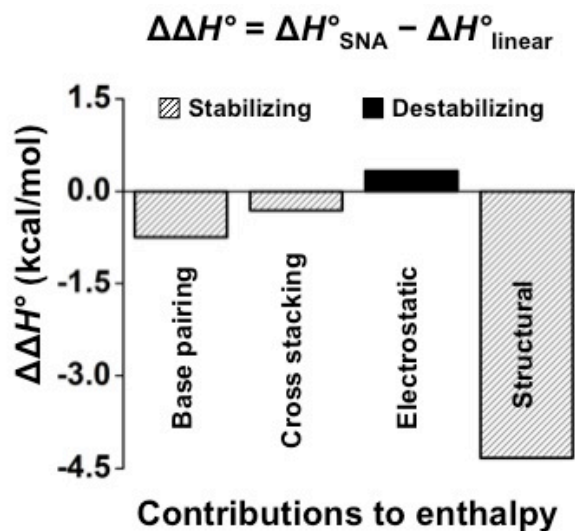


Figure 2.9. Break-down of contributions to the difference in enthalpy of hybridization between an SNA and a linear DNA strand derived from implicit-ion coarse-grained MD simulations.

Further analysis of the structural energy for the nanoparticle-bound DNA strand demonstrates that the enhancement relative to the linear DNA is most pronounced for the T₁₀-linker region of 10 thymine bases that connects the duplex to the nanoparticle surface (Figure 2.10). This T₁₀ single-stranded linker region became more ordered and therefore structurally stabilized by ~0.6 kcal/mol after hybridization (Figure 2.10B). Additionally, the entire nanoparticle-bound strand experienced a hybridization-induced structural stabilization ~2.2 kcal/mol greater than the stabilization observed in the linear case (Figure 2.10C). If the stabilization experienced by the T₁₀ region is subtracted, the remaining ~1.6 kcal/mol must originate from the structural stabilization (more energetically favorable angles, dihedrals, and base stacking) of the DNA junction region, which connects the duplex to the T₁₀ linker.

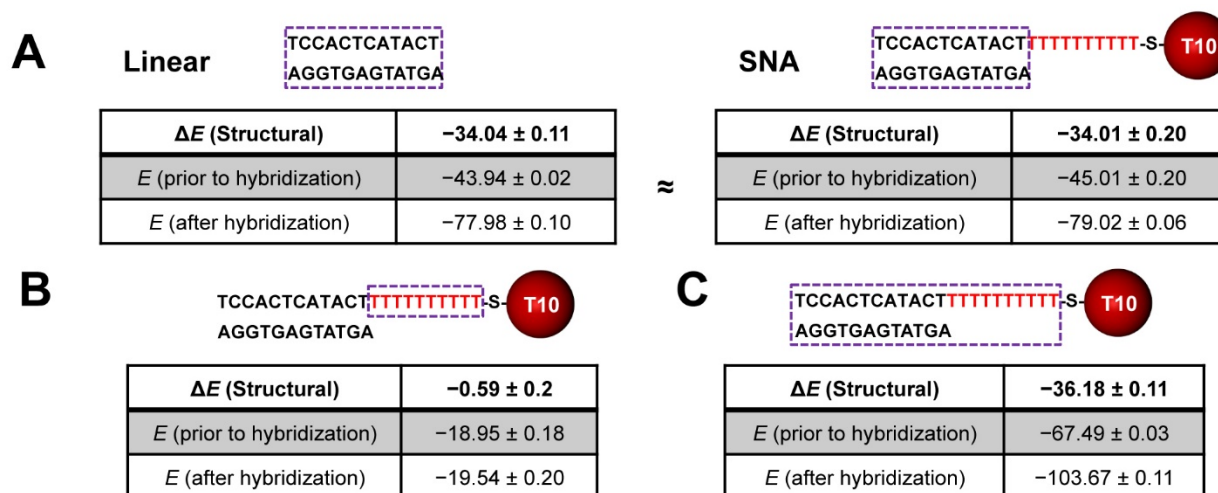


Figure 2.10. Comparison of the structural energy obtained from implicit-ion simulations of the nanoparticle-attached DNA strand before and after hybridization. The strand region for which the structural energy was calculated is enclosed in a purple dashed box, (A) the duplex region for both the linear and SNA systems (B) the single-stranded T₁₀ linker region that associates the duplex to the SNA and (C) the entire particle-bound DNA strand. All energies are given in units of kcal/mol.

Based on these findings, it is possible that the single-stranded T₁₀ linker region alone and not the SNA architecture is responsible for the observed enthalpic binding enhancement. To determine the contribution of the T₁₀ linker region to linear strand hybridization, the heat of complementary strand association with a linear 12-merT₁₀ was measured (Figure 2.11). Within error, the presence of the T₁₀ linker did not affect the enthalpy of hybridization for the linear DNA. Therefore, we conclude that the SNA architecture must give rise to the change $\Delta\Delta H$ in the structural hybridization energy. Confinement due to surface attachment and molecular crowding prevents hybridized DNA on the nanoparticle from adopting energetically unfavorable conformations that cause distortions in the bond angles, dihedrals, and intra-strand base stacking

away from the minimum-energy conformation, as would occur in the unconfined linear DNA case.

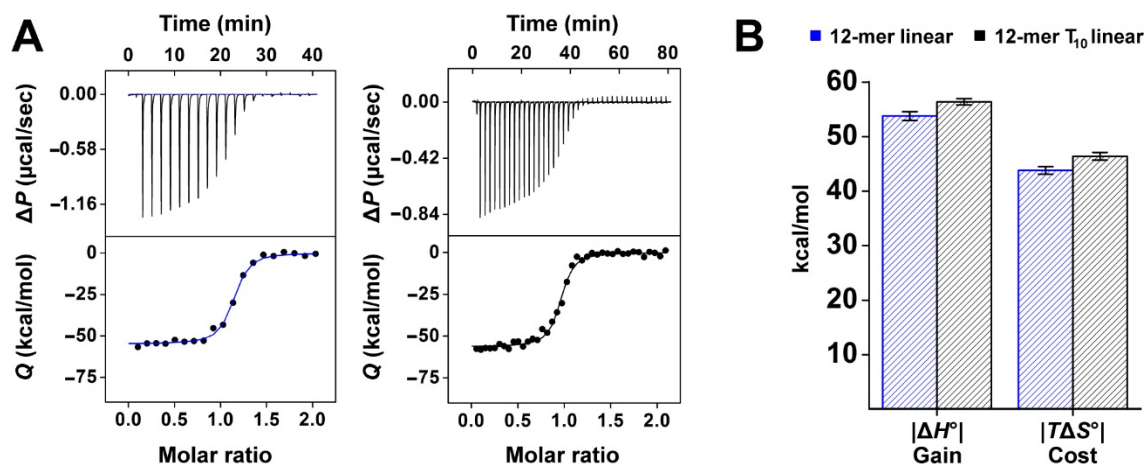


Figure 2.11. (A) Comparison of ITC data and (B) break-down of enthalpic and entropic contributions for the linear 12-mer (blue) and the linear 12-mer T₁₀ (black). See Table 3.3 for values. A: Upper panels: differential heating power ΔP vs. time; lower panels: integrated heats of reaction Q vs. molar ratio.

This unexpected finding is reminiscent of the stability observed for locked nucleic acid (LNA) hybridization. LNA is a synthetic RNA analog for which the ribose moiety is structurally constrained by a 2' oxygen to 4' carbon methylene bridge.⁸⁴ Incorporation of LNA bases into DNA oligomers has a demonstrated enhancement on the thermodynamic stability of duplexes.⁸⁵ This effect is enthalpically dominated, as shown by calorimetry,⁸⁶ and is thought to result from the conformational restriction of base-stacking and hydrogen bonding interactions.^{87,88}

2.3.4 Less confined SNA Architectures Have Less Favorable Enthalpy of Hybridization in Support of the Structural Confinement Hypothesis.

To test if DNA confinement on the surface of the nanoparticles indeed resulted in an enhanced enthalpy of hybridization, as suggested by the MD simulations, we performed ITC on two SNA systems with less confined DNA (Figure 2.12). We hypothesized that if conformational restriction of duplexes on the SNA resulted in an enhanced enthalpy of hybridization, then less confined SNA duplexes should have a less favorable enthalpy of hybridization. First, we decreased the DNA surface density by functionalizing nanoparticles with only 30 DNA strands, to obtain a density 33% lower than that of the original SNAs (Figure 2.12A). In support of our hypothesis, the hybridization enthalpy of the first 4 DNA strands on these low-density SNAs was 6.4 ± 2.7 kcal/mol less favorable. To further explore the degree to which confinement on SNAs could be tuned, we tested an SNA architecture with an even lower degree of confinement. We moved the duplex-forming region of the DNA further away from the nanoparticle surface by replacing the T₁₀-linker region with a linker region of 30 thymine bases (T₃₀). For this design, we maintained the high DNA density of ~46 strands per particle. The increased distance from the nanoparticle surface caused a striking decrease in the enthalpy of duplex formation of 16.0 ± 2.8 kcal/mol (Figures 2.12B). The effect was so strong that nearly all enhancement of the enthalpy disappeared, with the enthalpy of hybridization on the T₃₀-SNA nearly identical to the enthalpy of hybridization of linear DNA. The combined density and linker data were corroborated by simulation (Figure 2.13) and demonstrated that the enthalpy of complementary DNA hybridization onto SNAs can be tuned by as much as 20 kcal/mol simply by varying the degree of confinement of a surface-bound strand.

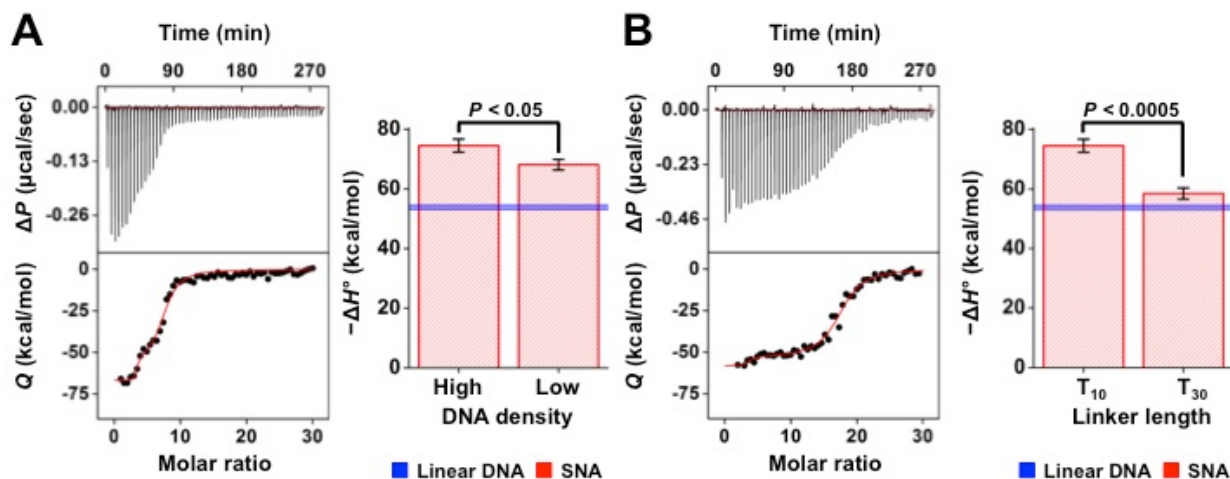


Figure 2.12. ITC (left) and enthalpy of hybridization (right) onto SNAs for the first 4 complementary strands for (A) low-density SNAs (~30 strands per particle) and (B) SNAs functionalized with 45 strands of longer, more flexible 12-mer T_{30} linker DNA. Upper panels: differential heating power ΔP vs. time, lower panels; integrated heats of reaction Q vs. molar ratio. Hybridization enthalpy for linear DNA (blue) and the original SNA (high/ T_{10}) are provided for comparison.

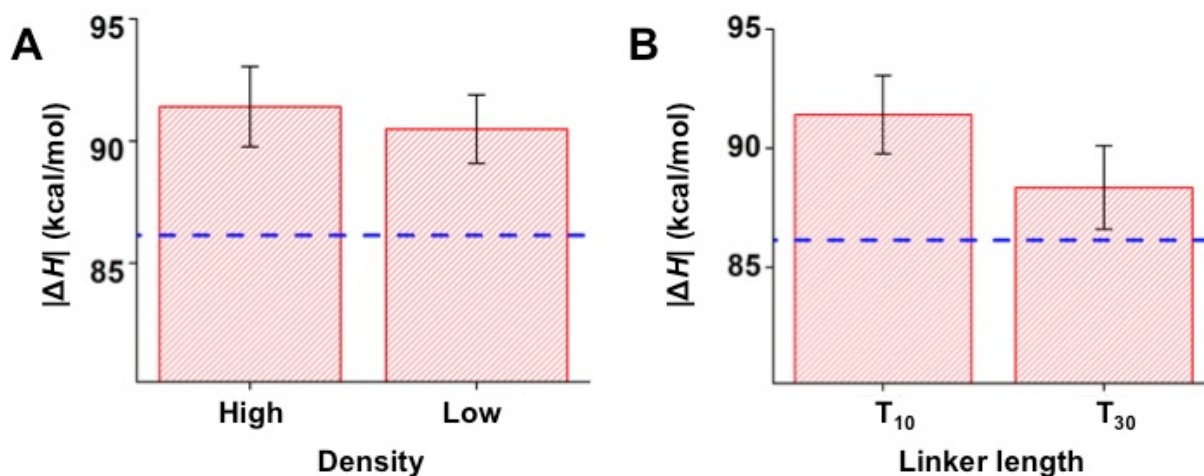


Figure 2.13. Comparison of hybridization enthalpies obtained from implicit-ion simulations for SNAs functionalized with different DNA (A) densities (High: 46 strands per particle, Low: 30 strands per particle) at fixed linker length (T_{10}) and (B) linker lengths (T_{10} and T_{15}) at a constant density of 46 strands per particle. The enthalpy of linear DNA hybridization is provided in blue for reference.

2.3.5 The large entropic cost incurred upon complementary strand hybridization to SNAs is also explained by structural confinement

Structural confinement also helps explain the considerable entropic cost upon complement hybridization on an SNA. In simulations, we found that upon hybridization single-stranded DNA surrounding the duplex on the surface became structurally more ordered (Figure 2.14). The total structural energy of the remaining DNA strands became more favorable by ~ 2 kcal/mol. This implies that all single-stranded DNA on the nanoparticle surface explored less unfavorable conformations after hybridization of one complement. While this effect was minor on a per-strand basis, collectively these contributions significantly reduced the ensemble degrees of freedom. This entropic cost counteracts hybridization of the first DNA strand on an SNA, but has been shown to reduce the entropic cost for subsequent hybridization events.²⁴

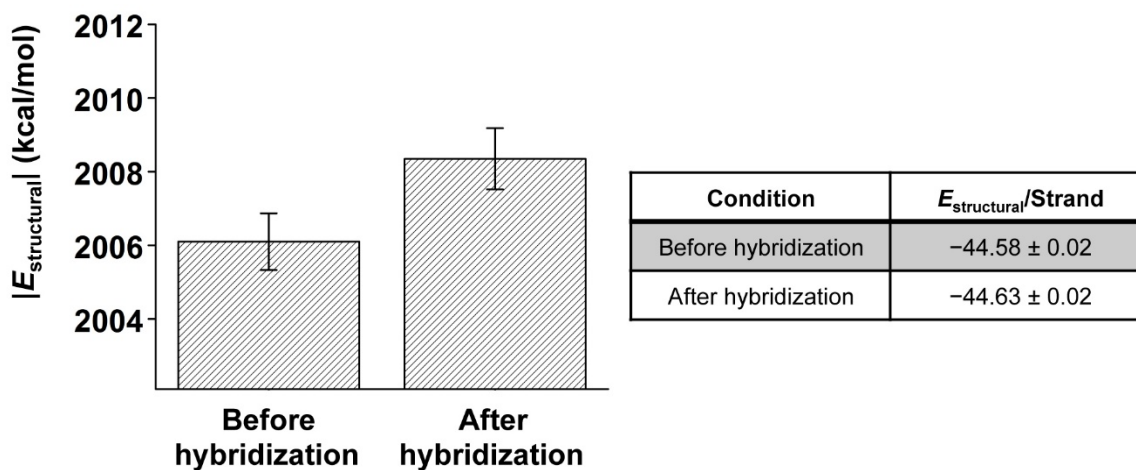


Figure 2.14. Comparison of the total structural energy obtained from implicit-ion simulations of the remaining 45 unhybridized nanoparticle-bound DNA strands before and after hybridization of a complement.

2.4 Conclusions

In conclusion, we have demonstrated that relative to linear DNA, the enthalpy of complement hybridization is more favorable on spherical nucleic acids and results in an enhanced free energy of binding. This work changes the way we think about DNA confinement on DNA-functionalized surfaces. While one could make intuitive arguments that the observed binding enhancement on SNAs is entropically driven, experimental and computational data show that it is an enthalpically driven process. This new insight can inform future engineering of DNA-functionalized surfaces. The surface architecture of SNAs can be modified to increase or decrease the enthalpic contributions to hybridization and consequently influence therapeutically and diagnostically relevant association constants.

2.5 Experimental Methods

2.5.1 DNA and SNA Synthesis and Purification

Oligonucleotides were synthesized using solid-phase phosphoramidite chemistry (MerMade-6, BioAutomation). Post synthesis, oligonucleotides were purified by reverse-phase high-performance liquid chromatography (RP-HPLC) on a Varian Microsorb C18 column (10 μm , 300 \times 10 mm).

Spherical nucleic acid gold nanoparticles (SNAs) were synthesized according to literature procedure.^{3,4} Thiol-modified DNA (\sim 0.13 μmol s) was reduced with a 0.1 M solution of DTT for one hour. DTT was removed by size-exclusion chromatography with a NAP5 column (GE Healthcare). Purified DNA was then added to a solution of 5.9-nm gold nanoparticles (25 mL of \sim 83 nM) that was sonicated for 10 seconds and allowed to shake at 40°C for \sim 1 hr. For the next \sim 3 hours, 0.1 M sodium phosphate buffer (pH 7.4), 0.1% SDS, and 2 M NaCl, were added to the nanoparticle-DNA solution at 30-minute intervals followed by sonication and shaking. Once the DNA-nanoparticle solution reached a final concentration of 0.01 M sodium phosphate, 0.01% SDS and 0.5 M NaCl, it was shaken for 12–16 hours at 40°C. Following functionalization, excess DNA was removed from solution by centrifugation with $>$ 50 kDa centrifugal filters (Amicon® Ultra-15). The SNAs were washed 3 times with 0.01% SDS and concentrated to a final volume of \sim 0.7 μL 0.01% SDS.

2.5.2 DNA Density Quantification on SNAs

The density of thiolated DNA on the surface of purified SNAs was determined by UV-Vis Spectroscopy (Cary 5000, Agilent). The concentration of nanoparticles and DNA was determined by the Beer–Lambert law ($A = \epsilon bc$), which relates absorbance to concentration. For the gold nanoparticles, an extinction coefficient of $\epsilon = 1.68\text{E}7$ ($\text{M}^{-1}\cdot\text{cm}^{-1}$) was used. To

determine the concentration of DNA, the gold nanoparticle core was oxidatively dissolved by exposure to KCN (150mM final concentration). A DNA absorbance standard curve was created for each sequence, taking into consideration the KCN and SDS concentrations in the unknown SNA samples. DNA density measurements were performed in triplicate for each SNA sample.

2.5.3 Fluorescence Hybridization Experiments

Fluorescence hybridization experiments were performed on a Jobin Yvon Fluorolog FL3-22 spectrofluorometer over a temperature range of 55°C to 21°C. Fluorescence measurements were made at 2-degree increments with a 10-minute equilibration time at each point. Samples were prepared over a range of concentrations (2–20 nM) of either linear DNA with a quencher (sequence 2) or SNAs (sequence 5). For linear DNA experiments, (Alexa Fluor 488) dye-labeled complementary DNA (sequence 4) was added in a 1:1 DNA molar ratio. In the case of the SNA, the complementary strand was added in a 1:1 ratio of complement to nanoparticle. Experiments were performed in triplicate at each sample concentration..

2.5.4 Treatment of the SNA as Single Entity for Analysis

This work treats the SNA as a single molecular entity rather than 46 individual DNA strands. This is why in the van 't Hoff analysis total concentration (C_T) is taken to be the sum of complementary DNA strands plus SNAs, and not total DNA concentration.

The choice to treat the SNA as a single entity comes from applications, where the target complementary nucleic acid of interest is often present at substoichiometric concentrations relative to the SNAs. In this scenario, the binding constant of the first binding event on the SNA “molecule” determines its efficacy as a diagnostic and not the valency-corrected binding constant. Therefore, in the van 't Hoff analysis we consider the functional valency of the SNA (1:1 binding), rather than the structural valency.

Treatment of the SNA as 46 individual DNA strands in the van 't Hoff analysis would not consider negative cooperativity observed in this system, because any site on any SNA is equally available for binding. At one extreme all strands on the SNA could be hybridized, which experiment shows does not occur due to each subsequent binding event being less favorable. Additionally, this treatment of the SNA as independent binding sites ignores the physical constraints placed on the DNA by covalently binding it to the nanoparticle. In this case, every DNA strand is able to freely explore the full volume of the container, which will have a large effect on the degrees of freedom of the system and greatly impact the entropy. On the contrary, treatment of the SNA as a single molecule inherently captures the sum of interactions from neighboring strands on the first binding event (the nature of those interactions can then be discerned from simulation) and accounts for the restriction in degrees of freedom the DNA experiences from surface attachment. Therefore, treating the SNA as single polydentate molecule can more appropriately describe the first hybridization event.

2.5.5 Isothermal Titration Calorimetry Experiments

ITC experiments to measure DNA hybridization enthalpy directly were carried out on a MicroCal (GE Healthcare) ITC200 isothermal titration calorimeter at 25°C..

All samples including the reference buffer were prepared with Nanopure™ water (18.2 MΩ), 0.01% sodium dodecyl sulfate (SDS), and 0.3 M sodium chloride (NaCl). Titrant and sample cell concentrations were modified to both capture early hybridization events and ensure sample saturation. See tables below for sample concentrations. For each experiment, an initial 0.1-μL injection was performed to counteract autotitrator backlash. For linear DNA, ITC experiments consisted of 19 2-μL injections of complementary strand into 280 μL of linear strands. For SNAs, 57 0.7-μL injections of complementary strands were made.

Sample	Sequences	[Linear DNA] in Sample Cell	[Complementary DNA]
12-mer Linear	1,3	20 μM	200 μM

Sample	Sequences	[NP] in Sample Cell	[Complementary DNA]
SNA_T ₁₀ 12-mer (high density)	3,5	0.714 μM	100 μM
SNA_T ₁₀ 12-mer (low density)	3,5	1.0 μM	100 μM
SNA_T ₃₀ 12-mer	3,6	0.714 μM	100 μM
SNA_T ₂₂	3,7	0.714 μM	100 μM

2.5.6 Simulation Model and Systems

We used the 3SPN.2 coarse-grained model,⁸² which has been carefully parametrized to reproduce correct structural, thermodynamic, mechanical, and kinetic properties of DNA. This model separates the DNA into three sites per nucleotide, one each for the phosphate, sugar, and base. It has been implemented in the LAMMPS molecular dynamics package and is available for download.⁶

To simulate the SNA, the nanoparticle was modeled by a single bead, which interacts with all the DNA sites via a shift-truncated Lennard-Jones potential,

$$E_{\text{NP-site}}(r) = \begin{cases} 4\epsilon \left[\left(\frac{\sigma_{\text{NP-site}}}{r} \right)^{12} - \left(\frac{\sigma_{\text{NP-site}}}{r} \right)^6 + \frac{1}{4} \right] & (r \leq r_c) \\ 0 & (r > r_c) \end{cases},$$

where $\epsilon = 0.26$ kcal/mol and the cutoff distance $r_c = 2^{1/6}\sigma_{\text{NP-site}} = 3.2$ nm, which is the sum of the radius of the nanoparticle (3.0 nm) and the average radius of DNA sites (0.2 nm). The nanoparticle-bound DNA sequence with a 12-base “sticky end” and a poly-thymine linker region (T₁₀ or T₁₅, sequence 5) and the complementary DNA (sequence 3) were designed to match experiment. To mimic the DNA density of experimental SNAs, 46 (high-density case) or 30 (low-density case) single-stranded DNA chains were grafted on the nanoparticle. The 3' end of

the DNA was bonded on the nanoparticle surface using rigid-body dynamics. The grafted DNA strands were distributed uniformly on the sphere following a triangular pattern.

2.5.7 Implicit-Ion Simulations Method

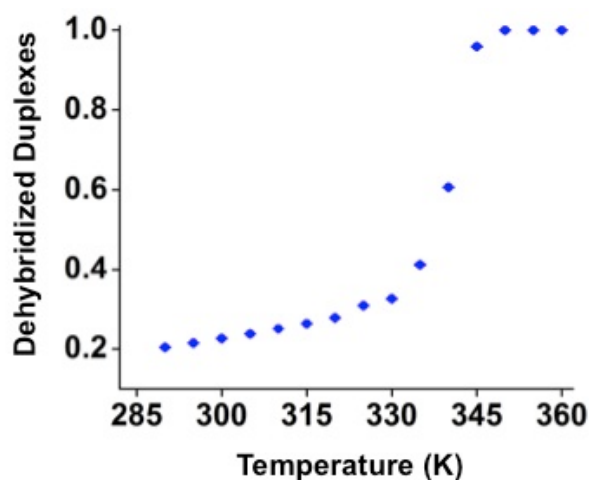
Molecular dynamics (MD) simulations with implicit ions were performed to mimic experimental conditions for both the linear DNA system and the SNA system. For the SNA system, we simulated a single DNA-grafted nanoparticle in a cell of linear size 132.4 nm. This cell size yielded a nanoparticle concentration of 0.714 μM . In the linear DNA system, the number of DNA strands was set to either 30 or 46 in order to match the concentration in the SNA system. The cell size was chosen to be 135.6 nm and 156.3 nm, respectively, to maintain the linear DNA concentration at 20 μM . The concentration in both cases was consistent with experiments.

All simulations were performed in the *NVT* ensemble using a Langevin thermostat in a 3D periodic cubic cell. All simulations were performed at 310 K (see discussion below concerning the choice of the simulation temperature) and at 0.3 M ionic strength. The Debye–Hückel approximation was used to model the interaction between phosphate sites, which carry a charge of -0.6 .⁸² All systems were simulated with a 10-fs time step for 50 ns during equilibration and a 20-fs time step for 1 μs during production. Ten independent runs were conducted for each condition to obtain ensemble averages.

2.5.8 Melting Curve Calculated from Implicit-Ion Simulations

To test the ability of this implicit-ion DNA model to predict thermodynamic properties of the relevant DNA sequences at an ionic strength of 0.3 M, we performed separate simulations to determine the melting curve of a linear DNA system consisting of 46 single DNA strands (sequence 1) and 46 complementary strands (sequence 3) at a concentration of 20 μM (for either

sequence 1 or 3). These simulations were started with 46 fully duplexed DNA strands and ran for 3 μ s of equilibration followed by 1 μ s of production with a 20-fs time step for both processes. We note that the system reached equilibrium very quickly (within 50 ns) when the temperature was away from the melting temperature. Yet, we imposed the extended 3- μ s equilibration period to guarantee equilibration at temperatures close to the melting temperature. The total number of complementary base pairs being formed n_{bp} was calculated at each time step, and the average fraction of dehybridized base pairs was given by $(1 - \frac{\langle n_{bp} \rangle}{12 \times 46})$, where the angular brackets denote the time average. This yields the computational melting curve:



The maximum slope of the melting curve yields a melting temperature around 340 K. The predicted melting temperature for linear DNA of this sequence at 20 μ M sample concentration and 0.3 M ionic strength is 326.4 K, as calculated using the OligoAnalyzer tool on the IDT website.⁷ Thus, our implicit-ion DNA model gave a melting temperature that was 4% higher than the nearest-neighbor prediction from the OligoAnalyzer tool. This increase of the melting temperature at higher ionic strength has been attributed to the use of the Debye–Hückel approximation.⁸ Because experiments were performed at room temperature (298 K), i.e., around

91% of the predicted melting temperature, we performed all implicit-ion simulations at 310 K (91% of the melting temperature of the simulation model) to make experiment and simulation comparable.

2.5.9 Calculation of Hybridization Enthalpy in Implicit-Ion Simulations

The hybridization enthalpy ΔH was calculated as the difference between the total energy of the system in the hybridized state (E_H) and the unhybridized state ($E_U + E_S$), as shown in Figure 2A of the main text. Specifically, for the unhybridized state of the linear DNA system, E_U is the total energy of 30 or 46 single strands of DNA (sequence 1), and E_S is the total energy of the complementary strand (sequence 3, box size 43.6 nm). To simulate the hybridized state, we replaced one single-stranded DNA in the multi-strand unhybridized system with a hybridized duplex (sequence 1 with sequence 3) and calculated the average total energy E_H after equilibration. Similarly, for the SNA system, the hybridized state refers to the system where one of the 30 or 46 grafted DNA chains has already formed a duplex with a complementary strand (sequence 3). The total energy of each state was obtained by taking the time average during each run and ensemble average over 10 independent runs.

2.5.10 Explicit-Ion Simulation Model and Procedure

MD simulations with explicit ions were also performed, both for the linear DNA system and for the SNA system. We again used the 3SPN.2 coarse-grained model, which has recently been extended to include explicit ions.⁸ Enough positive counterions (Na^+) to compensate for the negatively charged phosphate sites on the DNA and 0.3 M NaCl salt were explicitly added to the system. Because the large number of ions significantly increased the simulation time, especially for large simulation cell sizes, we maintained the box size at 50 nm in both cases. For the SNA system, we simulated a single nanoparticle with 46 grafted DNA chains (linker region T_{10}),

resulting in a nanoparticle concentration of 13.29 μM . For the linear DNA system, we included 10 DNA chains in the box, resulting in a DNA concentration of 132.85 μM .

All simulations were performed at 298 K (room temperature), with a 10-fs time step for 100 ns of equilibration and a 20-fs time step for 1 μs of production. Five independent runs were conducted to obtain an ensemble average. All other parameters were identical to those used in the implicit-ion simulations.

2.5.11 Calculation of Hybridization Enthalpy in Explicit-Ion Simulations

The hybridization enthalpy ΔH in the explicit-ion simulations was calculated as the difference between the total energy of the system in the hybridized state (E_H) and the unhybridized state (E_U). In contrast to the implicit-ion simulations, we did not take into account the total energy of a single complementary target (E_S) when determining the unhybridized state. We reasoned that since E_S contains the ion–ion interaction energy it should not be added to E_U . Since the same E_S applies to the SNA hybridization and the free DNA hybridization, this choice has no effect on the calculation of the *difference* in hybridization enthalpy, $\Delta\Delta H$, but it does affect the quoted values for the hybridization enthalpies themselves.

For the unhybridized state of the linear DNA system, E_U is the total energy of 46 single strands of DNA (sequence 1). To simulate the hybridized state, we replaced one single-stranded DNA in the unhybridized system with a hybridized duplex (sequence 1 with sequence 3) and calculated the total energy E_H after equilibration. Similarly, for the SNA system, the hybridized state refers to the system where one of the 46 grafted DNA chains has already formed a duplex with a complementary target (sequence 3). The total energy of each state was obtained by taking a time average for each run and an ensemble average from five independent runs.

CHAPTER 3: The Role of Surface Attachment on the Enthalpy of DNA

Displacement Reactions

3.1 Summary

DNA displacement reactions have enabled the design of robust *in vivo* RNA probes and DNA-based dynamic materials, relying on the idea that displacement is thermodynamically favorable. The thermodynamic propensity for displacement is a parameter that is usually fixed in the design of new diagnostic probes, because it relies on changes in DNA sequence, which would inhibit detection of specific sequences. In this work we demonstrate that the thermodynamic propensity toward displacement is easily tuned on the surface of spherical nucleic acids (SNAs), which are gold nanoparticles that are densely functionalized with radially oriented DNA (Figure 3.1). The tunability of the SNA architecture with DNA density, distance from the nanoparticle surface and nanoparticle radius of curvature imparts tunability in the thermodynamic propensity of DNA displacement reactions from surfaces. Isothermal titration calorimetry is used to demonstrate that the enthalpy of displacement can be tuned by as much as 20 kcal/mol, simply by changing the SNA architecture. This work informs the design of more sensitive *in vivo* probes of RNA for which DNA sequence is difficult to modify.

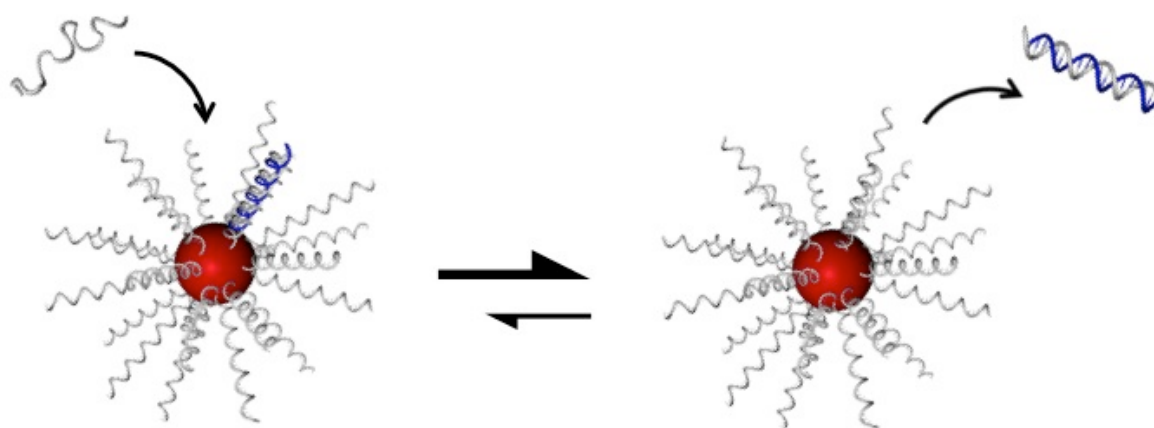


Figure 3.1. Scheme illustrating a DNA displacement reaction from a spherical nucleic acid

3.2 Introduction

DNA displacement reactions are ubiquitous for biological applications and the design of dynamic materials.^{33,39–41,47,63,65,89–91} A displacement reaction takes place when one DNA strand hybridizes its complement in solution and in the process displaces one or more pre-hybridized strands.⁹¹ The driving force for this reaction is a greater degree of complementarity between the newly hybridizing DNA strands relative to the pre-existing duplex. Therefore, a single-stranded toehold region where displacement can initiate and proceed through branch migration must be incorporated into the DNA design of materials based on displacement reactions. Access to certain applications, such as nucleic acid sensing and tracking, are fundamentally limited by this design requirement, because the relevant targets are disease markers of fixed sequence.

Spherical nucleic acids (SNAs), nanoparticles densely functionalized with linear DNA,^{1,2} can address this limitation. Changes in SNA architecture have been shown to modulate the thermodynamics of DNA hybridization (chapter 3) and should translate to comparable changes in the thermodynamics of displacement reactions.

Herein, we employ isothermal titration calorimetry (ITC) to demonstrate that the thermodynamics of DNA displacement reactions on SNAs is far more tunable than the thermodynamics of linear DNA displacement. By changing nanoparticle radius of curvature, DNA surface density, and DNA distance from the surface, the enthalpy of DNA displacement can be modified by 10-20kcal/mol without ever changing the DNA sequence.

3.3 Results and Discussion

3.3.1 Linear DNA Experiment Reveals the Feasibility of Using ITC to Study Displacement Reactions

To determine the feasibility of using ITC to study DNA displacement, a model linear DNA system was tested. ITC experiments measure heat released or absorbed during a reaction occurring at constant temperature, and therefore provide a direct measure of reaction enthalpy^{75,76}. In displacement reactions, the enthalpy of association is the most relevant parameter, as it is the large enthalpic gain that drives the reaction forward. Two informative experiments were carried out, a hybridization experiment to associate a long, 21-base, strand with a short, 12-base, strand (Figure 3.2A), and a displacement experiment where the full, single-stranded complement was titrated into a solution with the pre-hybridized duplex to displace the short strand. (Figure 3.2B). The sequences were designed to have minimal secondary structure, and the degree of overlap between strands was chosen for maximal signal without exceeding the limitations of the ITC.

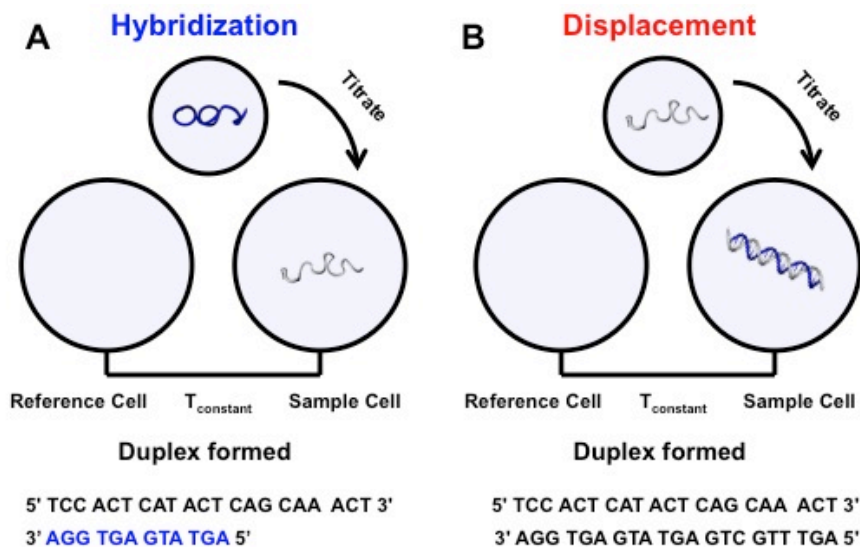


Figure 3.2. Scheme illustrating the ITC experiments to extract thermodynamic constants from displacement reactions. (A) Hybridization takes place when a 21mer hybridizes a 12mer complement. (B) Displacement takes place when a 21-mer complement displaces the pre-bound 12mer.

Analysis of ITC-derived enthalpies (Figure 3.3, Table 3.1) reveals that displacement experiments are feasible. Experimental enthalpies were compared to enthalpy values derived from a nearest-neighbor model, which gives the thermodynamic constants of idealized duplexes.²⁷ While the hybridization enthalpy value (-77.2 ± 0.9 kcal/mol) agreed well with the calculated value (-79.2 kcal/mol) the experimental displacement value (-59.4 ± 0.4 kcal/mol) deviated significantly from the calculated value (-68.2 ± 0.4 kcal/mol). A control experiment to determine the enthalpy of just the remaining 9-mer duplex showed that the measured displacement enthalpy is within the expected experimental value.

Table 3.1. Enthalpies of linear DNA displacement experiments

Duplex	Enthalpy (kcal/mol)
5' TCC ACT CAT ACT CAG CAA ACT 3' 3'AGG TGA GTA TGA GTC GTT TGA 5'	-149.8 ± 0.5
5' TCC ACT CAT ACT CAG CAA ACT 3' 3'AGG TGA GTA TGA 5'	-77.2 ± 0.9
5' TCC ACT CAT ACT CAG CAA ACT 3' 3' GTC GTT TGA 5'	-57.5 ± 0.6
Displacement Experiment	-59.4 ± 0.4
5' TCC ACT CAT ACT CAG CAA ACT 3' Dilution	-1.6 ± 0.2
3'AGG TGA GTA TGA GTC GTT TGA 5' Dilution	-3.6 ± 0.8

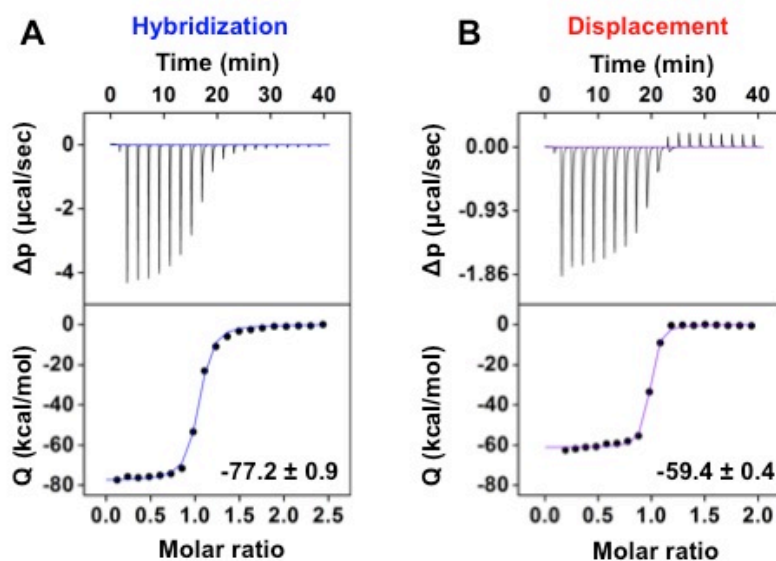


Figure 3.3. ITC plots of (A) the hybridization experiment and (B) the displacement experiment with linear DNA strands.

3.3.2 SNA Displacement Experiments Confirm Binding Enhancement Relative to Linear DNA

With confidence in the feasibility of the displacement experiments for linear DNA, SNA experiments were carried out. In this case, the short 12-base strand is on the SNA, while the 21-base strand is hybridizing. Upon addition of the full 21-base complement, the SNA would be displaced. Previous work has shown that the enthalpy of hybridization onto 5.9nm gold SNAs functionalized with ~ 45 strands per particle is enhanced relative to linear DNA hybridization. We hypothesized that if a similar SNA architecture was used for our displacement experiments, the enthalpy of hybridization would be enhanced and that of displacement would be lower than in the linear case. The enthalpy of hybridization for a 5.9nm SNA functionalized with 41 ± 1 strands per particle is indeed enhanced by 8.0 ± 0.9 kcal/mol (Figure 3.4, Table 3.2). Surprisingly, so is the enthalpy of displacement. The reasons behind this enhancement are unknown, but probably result from the SNA architecture itself.

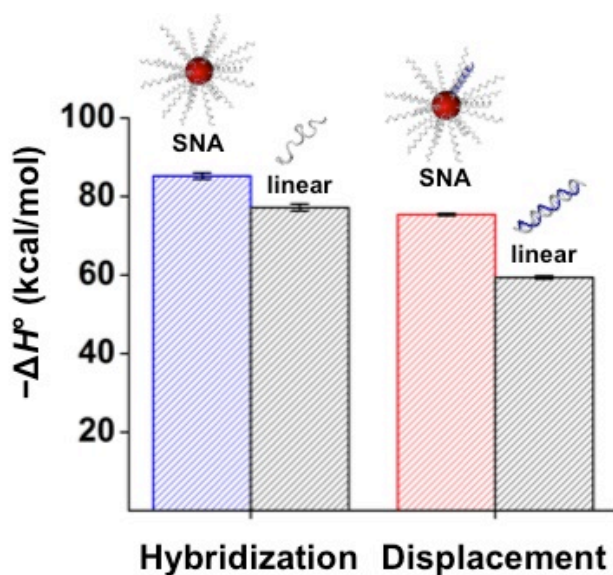


Figure 3.4. ITC-derived enthalpy values for the hybridization (blue) and displacement (red) from a 5.9nm SNA functionalized with 41 strands per particle. For the displacement experiment, each particle is prehybridized with ~4 strands. The linear DNA values are provided in black for reference.

3.3.3 The Versatility of the SNA Architecture in Directing Displacement Reactions is Tested

To further probe the versatility of the SNA architecture to affect the thermodynamics of displacement reactions, the duplex region of the SNA was distanced from the nanoparticle surface with a T₃₀ linker region. This has been shown to greatly decrease the confinement of the DNA and therefore make the enthalpy of hybridization to the SNA less favorable. A less favorable enthalpy of hybridization should result in a more favorable enthalpy of displacement. Indeed, the hybridization enthalpy is less favorable on the more flexible linker SNA, and the displacement concomitantly less favorable (Figure 3.5, Table 3.2). What is exciting about this result is the ability to tune both the hybridization and the displacement enthalpy without ever changing the sequence of the hybridizing moieties.

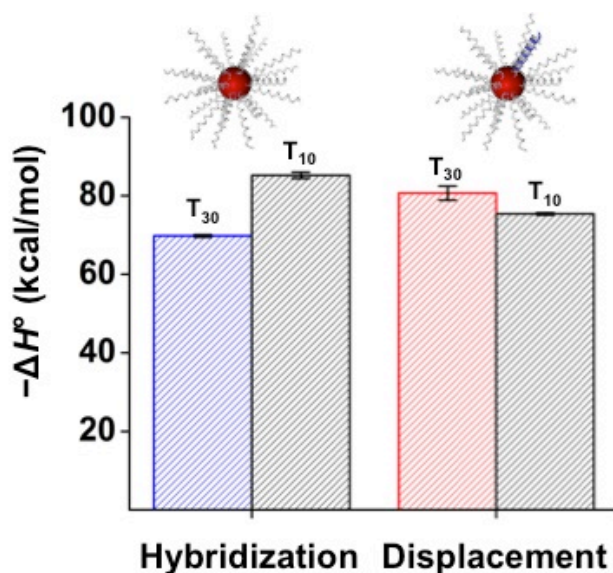


Figure 3.5. ITC-derived enthalpy values for the hybridization (blue) and displacement (red) from a 5.9nm SNA functionalized with 46 (T_{30}) strands per particle. For the displacement experiment, each particle is prehybridized with ~ 4 strands. The T_{10} SNA values are provided in black for reference.

Table 3.2. ITC derived enthalpy values for hybridization and displacement of different SNA constructs and linear DNA for comparison

Sample	Hybridization ΔH° (kcal/mol)	Displacement ΔH° (kcal/mol)
5nm T10	-85.2 ± 0.8	-75.4 ± 0.3
5nm T30	-69.8 ± 0.3	-80.7 ± 1.9
10nm T10	-81.5 ± 0.6	-84.5 ± 1.3
20nm T10	-72.6 ± 0.8	-104.0 ± 1.2
Linear	-77.2 ± 0.9	-59.4 ± 0.4

3.3.4 Determining the Role of Radius of Curvature on Displacement Reactions from SNAs

One of the reasons to understand displacement reactions on surfaces is to inform the design of nanoflare probes. Nanoflares are SNA-based intracellular detection agents that rely on displacement reactions for sensitive, fluorescence-based detection of mRNA.^{39–41,89} The

sensitivity of nanoflares could be improved to enable detection of RNA at low abundance by moving to an anisotropic nanoparticle core. This endeavor requires an understanding of how DNA displacement reactions vary with the radius of curvature of the nanoparticle core, as anisotropic nanoparticles tend to be bound by flat surfaces. In order to probe the role of radius of curvature on the thermodynamics of displacement reactions, three SNAs of different sizes (5.9, 9.5, and 19.7nm diameter) were synthesized with similar densities (~ 0.4 strands/nm²). Hybridization and displacement experiments were carried out and their values compared (Fig 3.6).

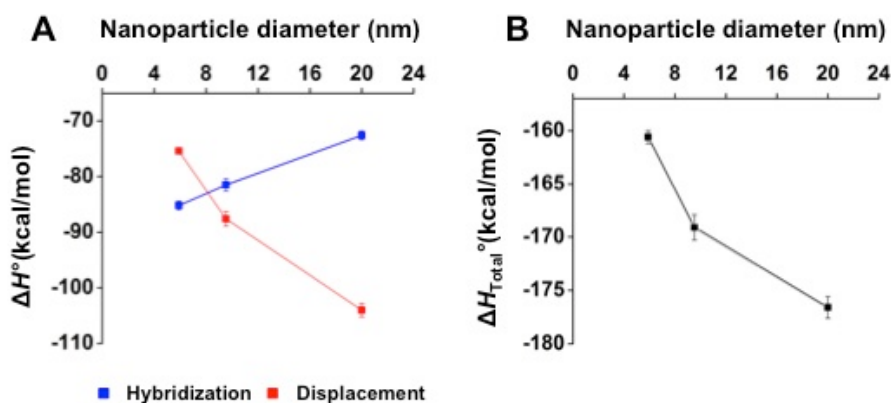


Figure 3.6. ITC-derived enthalpy values for (A) the hybridization (blue) and displacement (red) from SNAs as a function of nanoparticle diameter. (B) The sum of hybridization and displacement enthalpy values to demonstrate the stabilization of the displacement reaction as a function of nanoparticle size.

The enthalpy of hybridization to an SNA is hindered as the diameter of the nanoparticles increases (Figure 3.6A). This is most likely due to electrostatic and steric repulsion between neighboring strands. With this decrease in the hybridization enthalpy, comes an increase in the displacement enthalpy as a function of nanoparticle diameter. This is to be expected, since the 21-base complement doesn't have to "pull" as hard on the pre-formed duplex to displace it. What is interesting about these results is that when the sum of the hybridization and displacement

enthalpies $\Delta H^\circ_{\text{Total}}$ is plotted as a function of nanoparticle diameter, the total enthalpy is enhanced with size. This is a surprising finding that is probably due to local concentration effects increasing with increasing nanoparticle size, but should be further investigated.

These results suggest, that while the enthalpy of hybridization on anisotropic nanoparticles may be worse, the propensity toward displacement will improve. For the design of anisotropic diagnostic probes careful consideration of whether to favor hybridization or displacement enthalpy will have to be made on a case-by-case basis.

3.4 Conclusions

In conclusion, we have demonstrated that DNA displacement reactions on the surface of spherical nucleic acids are highly thermodynamically tunable. By varying the DNA linker flexibility and the nanoparticle radius of curvature, the displacement enthalpy can be tuned by more than 20kcal/mol without ever changing the hybridizing DNA sequence. Interestingly, we find that the overall stability of the system increases when displacement occurs on a surface rather than in the linear case. This is a phenomenon that is difficult to rationalize, but deserves careful consideration. The effect of radius of curvature on displacement reactions is stark, and informs the design considerations of probes that rely on DNA hybridization onto less curved nanoparticle surfaces.

CHAPTER 4: Understanding the Nanoparticle-Mediated Nucleation

Pathways of Anisotropic Nanoparticles

Portions of this chapter are adapted from *Chem. Phys. Lett.*, **2017**, 683, 389-392

Collaborators: Christine Laramy, Matthew Jones, Matthew O'Brien,

George Schatz and Chad Mirkin

4.1 Summary

Seed-mediated synthesis is a powerful technique to achieve highly uniform nanoparticles, wherein a preformed nanoparticle (“seed”) templates the growth of nanoparticle products via heterogeneous nucleation. Despite the success of this approach for a library of shapes, several anisotropic nanoparticle syntheses still yield broad product distributions with multiple defect structures. These shortcomings challenge the role of the nanoparticle precursor as a seed for certain syntheses and suggest the possibility of alternate nucleation mechanisms. We report a method to probe the role of the nanoparticle precursor in anisotropic nanoparticle nucleation with compositional and structural “labels” to track their fate. We use the synthesis of gold triangular nanoprisms (prisms) as a model system, as its product distribution includes products with at least two distinct defect structures. Rather than acting as a heterogeneous template, we find that the seed catalyzes homogeneous nucleation of prisms. An electron transfer mechanism is proposed as an alternative role of the nanoparticle precursor. This work shows that the chemical nature of the nanoparticle precursor can play a dominant role in dictating the product nucleation pathway, and provides a platform for achieving usable yields of highly anisotropic nanoparticle building blocks.

4.2 Introduction

The “seed-mediated” approach to nanoparticle synthesis has enabled reproducible control of nanoparticle structure and dramatic improvements in nanoparticle uniformity over earlier synthetic techniques.^{92–97} In this approach, pre-formed nanoparticle “seeds” are added to a solution of atomic precursors in the presence of a molecular reducing agent, as a means to spatiotemporally separate particle nucleation (*i.e.* seed formation) from growth (Figure 4.1). The underlying hypothesis of this approach centers on the use of nanoparticle precursors that act as static structural templates for heterogeneous nucleation. This hypothesis is supported by experiments that show a strong relationship between the size, shape, and defect structure of seeds and products.^{94,96–101}

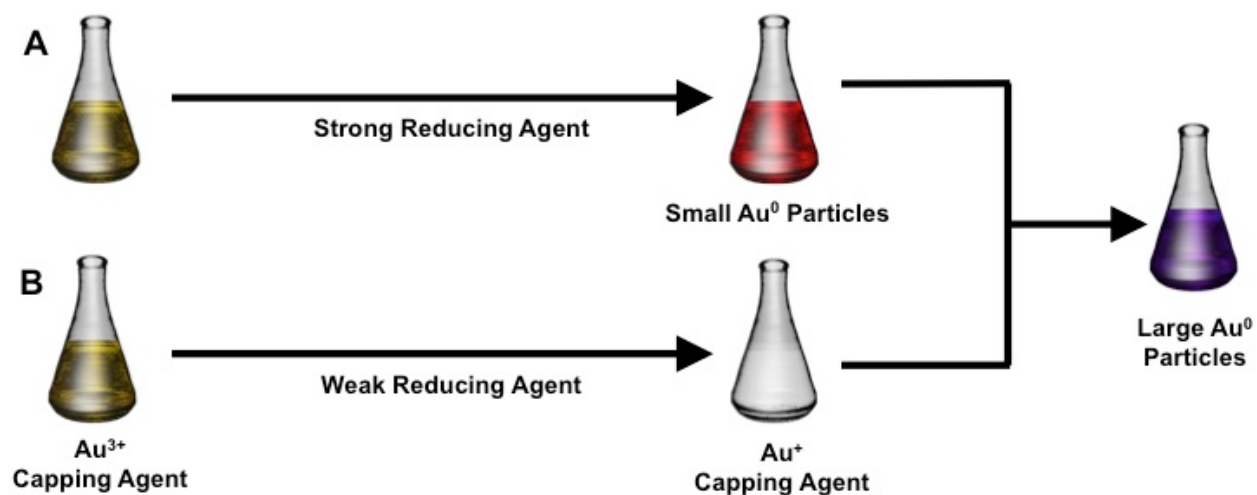


Figure 4.1. Scheme illustrating the seed-mediated synthesis technique where (A) a small nanoparticle “seed” is formed by fast reduction of metal precursor separate from a (B) growth solution of partially reduced metal precursor. Addition of the preformed “seed” to the growth solution promotes nucleation and subsequent nanoparticle growth.

However, certain “seed-mediated” syntheses remain limited by product distributions with multiple defect structures suggesting that, in some cases, the nanoparticle precursors may “mediate” nanoparticle growth in a reaction-dependent, rather than universal manner.^{102–104} The synthesis of gold triangular prisms (prisms) poses an interesting example of this phenomenon.^{61,105} While many prism syntheses make use of nanoparticle precursors, it is unclear what role these precursors play.^{61,106–108} One possibility is that they act as structural templates (i.e. seeds) for heterogeneous nucleation. Two primary pieces of evidence have been used to support this hypothesis: 1) addition of particle precursors initiates the growth of prisms and 2) the size of the prisms can be tailored through careful changes in the relative concentrations of particle and gold ion precursors.¹⁰⁵ An alternative, and more intriguing, possibility for the role of the precursor is suggested by several striking differences that exist in the synthesis of prisms relative to other seed-mediated syntheses. The products of this reaction differ in their defect structure: prisms have a planar-twinned defect structure parallel to their {111}-triangular cross-section,¹⁰⁷ while other products possess a multiply-twinned defect structure (decahedra and icosahedra).¹⁰⁹ Further, there are many syntheses with diverse reducing agents, capping ligands, shape-directing additives, nanoparticle precursor defect structures, or no nanoparticle precursors at all that produce prisms as products. This suggests that arguments for crystal facet blocking and “seed” defect structure being responsible for anisotropic particle growth may not fully explain the growth of prisms.^{92,100,106,107,110–113} Additionally, recent work has shown that multiple chemical equilibria can compete at a particle surface beyond the simple reduction of additional material.^{94,114} This led to the hypothesis that nanoparticle precursors play a more intricate chemical role beyond simply templating growth in the nucleation of prisms.

Herein, the synthesis of prisms is used as a model system to systematically explore the role of the nanoparticle precursors as a function of their composition and shape.⁶¹ In each experiment, the prism synthesis “growth solution” remains constant while nanoparticle precursor morphologies, defect structures, and compositions are deliberately varied to track the fate of the nanoparticle (Figure 4.2).

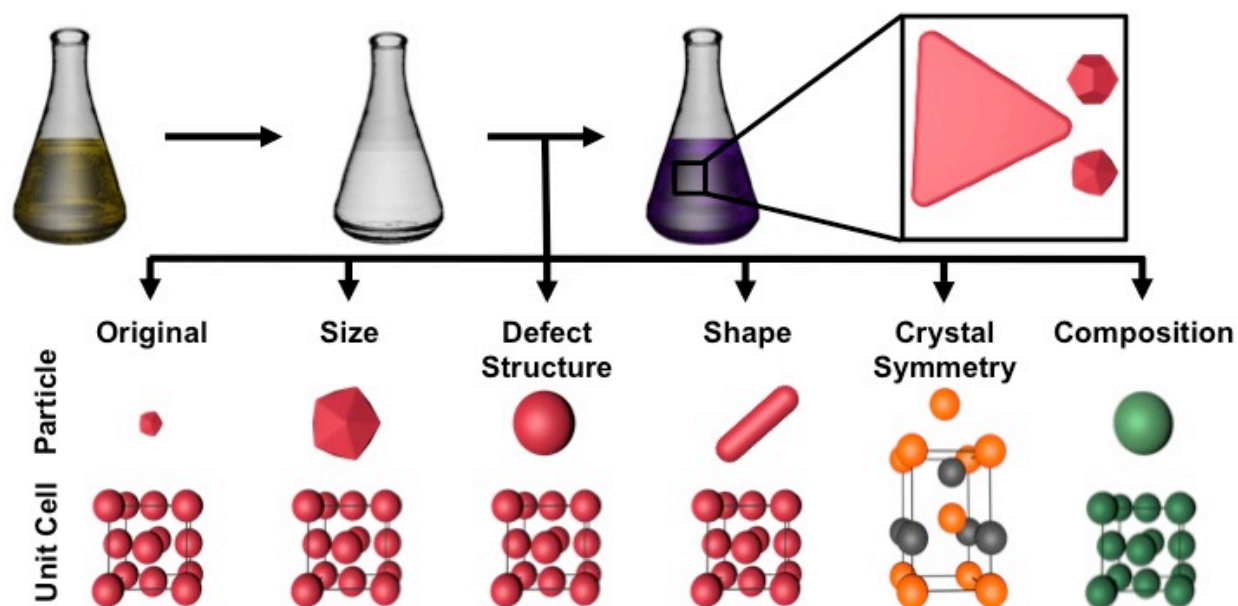


Figure 4.2. Scheme illustrating how the nucleation pathway of gold triangular prisms can be probed by systematically substituting different nanoparticle precursors under identical reaction conditions and characterizing the final product distribution.

The current understanding of seed-mediated synthesis implies that the defect structure of the initial seeds determines the potential reaction products. In the case of prisms, this implication suggests that some population of nanoparticle precursors must have a planar twinned defect structure in order to template planar twinned products.¹¹⁵ To directly test this understanding in the prism synthesis, the original nanoparticle precursors⁶¹ - a heterogeneous mixture of particles that vary in size and defect structure – were substituted for uniform, well-characterized particles (Figure 4.3). The size and shape of all particle precursor populations were rigorously characterized using software that enables quantitative analysis of electron microscopy images of $\sim 10^3$ particles per sample.¹¹⁶

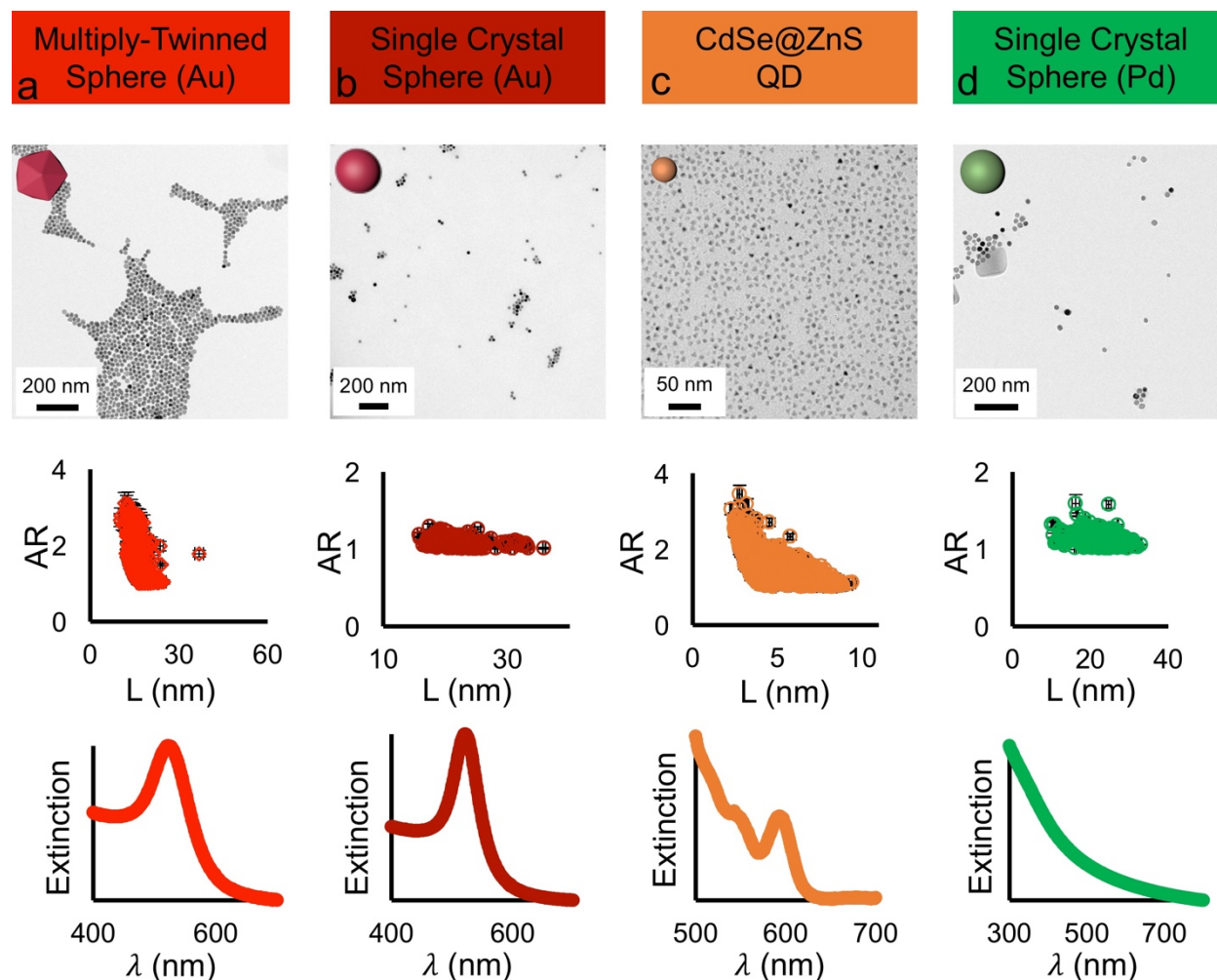


Figure 4.3. Characterization of nanoparticles for use as precursors in prism growth. (Top) Representative electron microscopy image of particles. (Middle) Algorithmic analysis of images to determine particle diameter (L) and aspect ratio (AR). (Bottom) UV-Vis spectroscopy of nanoparticles. a) Multiply-twinned gold particles purchased from Ted Pella. Middle plot shows algorithmic analysis of images of 1,667 particles ($d = 16.3 \pm 1.8$ nm). b) Single crystalline gold spheres synthesized in-house. Middle plot shows algorithmic analysis of images of 364 particles ($d = 22.5 \pm 3.0$ nm). c) CdSe@ZnS particles purchased from Invitrogen. Middle plot shows algorithmic analysis of images of 1,997 particles (5.7 ± 1.5 nm). d) Single crystalline palladium synthesized in-house. Middle plot shows algorithmic analysis of 657 particles ($d = 22.7 \pm 3.9$ nm).

4.3 Results and Discussion

4.3.1 Changes in Nanoparticle Precursor Size and Defect Structure do not Preclude

Formation of Prisms

The products from prism syntheses performed with multiply-twinned and single-crystalline particle precursors were first directly compared. To minimize the effect of high mobility of surface atoms in small nanoparticles (~ 5 nm), large (~ 20 nm) gold particles were used.^{117,118} Interestingly, substitution of small particle precursors for large multiply-twinned or single-crystalline particles both produced prisms (Figures 4.3a,b and 4.4). This experiment suggests that particle precursor defect structure does not dictate product formation in this synthesis. Further, atomic force microscopy (AFM) of prisms grown from multiply-twinned gold particles reveals that prisms are thinner than the initial particle precursors (Figure 4.5). Therefore, these results suggest that prisms may not be templated by heterogeneous nucleation onto “seeds”, but instead result from homogeneous nucleation and subsequent growth.

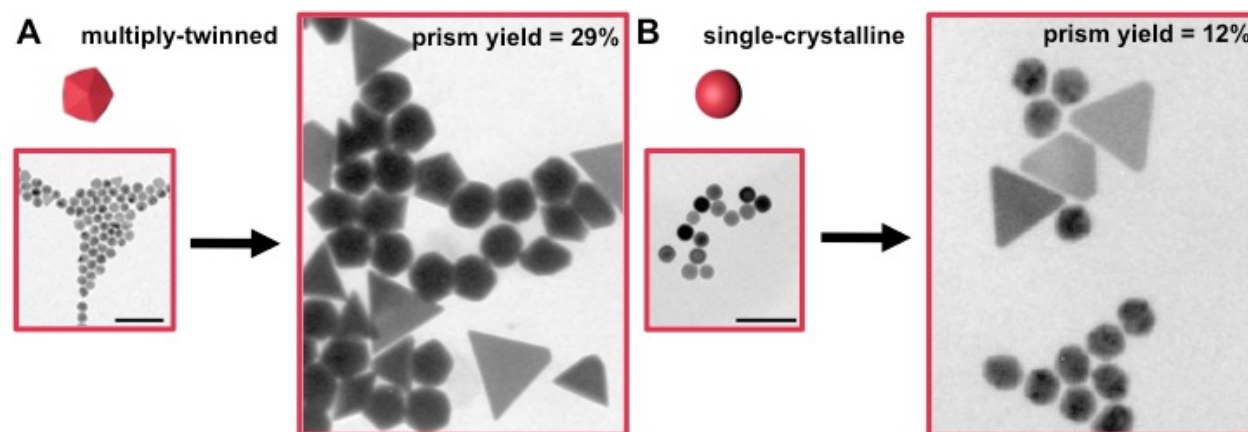


Figure 4.4. Gold nanoprism synthesis performed with (A) 17 ± 1.6 nm gold multiply twinned nanoparticles and (B) 26 ± 1.6 nm gold single-crystalline nanoparticles as precursors. Scale bars represent 100nm.

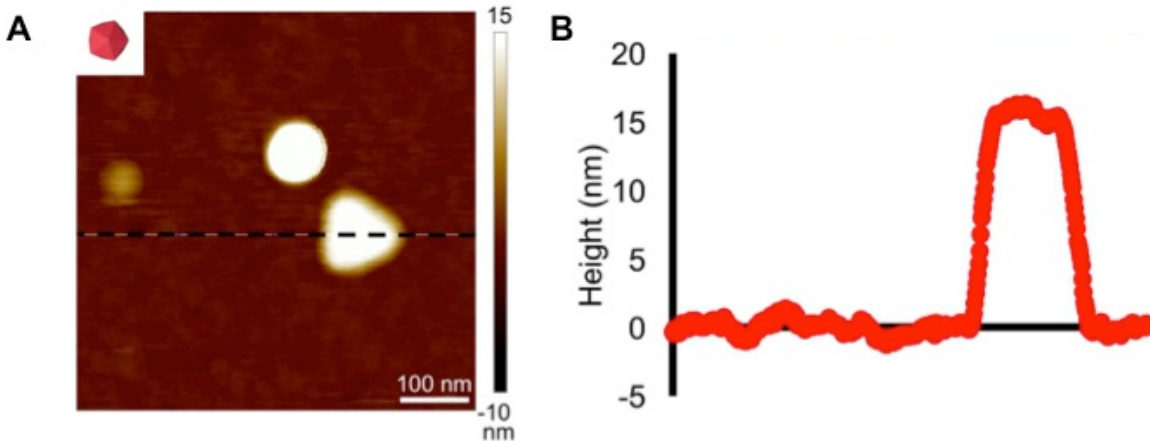


Figure 4.5. AFM analysis of prisms grown from large multiply-twinned gold nanoparticles ($d = 16.3 \pm 1.8$ nm) shows that the prism and CTAB bilayer have a combined height of 15.6 nm. (A) Height map of prism and pseudospherical impurity product. (B) Height at every point along dashed line in a.

4.3.2 Successful Synthesis of Prisms with Quantum Dot Precursors Suggest a Homogeneous Nucleation Mechanism

In order to directly test the hypothesis that prisms form as a product of homogeneous nucleation, the original gold nanoparticle precursor was substituted with a particle that would make heterogeneous nucleation and subsequent epitaxial growth of gold onto its surface energetically unfavorable. Wurtzite CdSe@ZnS quantum dots (QDs) were chosen as a substitute, as they have a large symmetry and lattice mismatch compared to FCC gold.¹¹⁹ Lattice mismatch is calculated by the following equation:

$$\% \text{ Lattice Mismatch} = \frac{a_{\text{surface}} - a_{\text{layer}}}{a_{\text{surface}}} \times 100\%$$

Therefore, the lattice mismatch between gold (FCC, $a=0.4078\text{nm}$) and ZnS (wurtzite, $a=b=0.3811\text{nm}$, $c = 0.6234\text{nm}$) is 7% in two dimensions and 34.6% in the third dimension. Although

there have been reports of epitaxial growth of FCC metals onto transition metal chalcogenide nanocrystals,^{120,121} such a large lattice mismatch makes epitaxy unlikely under the mild, aqueous conditions of the prism synthesis. Interestingly, with wurtzite QD precursors, this synthesis produced prisms in yields comparable to those using the original gold particles, 29% (Figure 4.6). Electron microscopy reveals circular holes and concave features on the prisms as well as pseudo-spherical impurity products. In addition, we observed the presence of small particles of low contrast relative to the prisms. Energy-dispersive X-ray spectroscopy (EDX) analysis of these particles indicates the presence of cadmium (Figure 4.6A). As expected, gold was found in the prisms as well as the pseudo-spherical impurity products, but no Cd was identified. These data support the hypothesis that prisms are products of a homogeneous nucleation growth pathway.

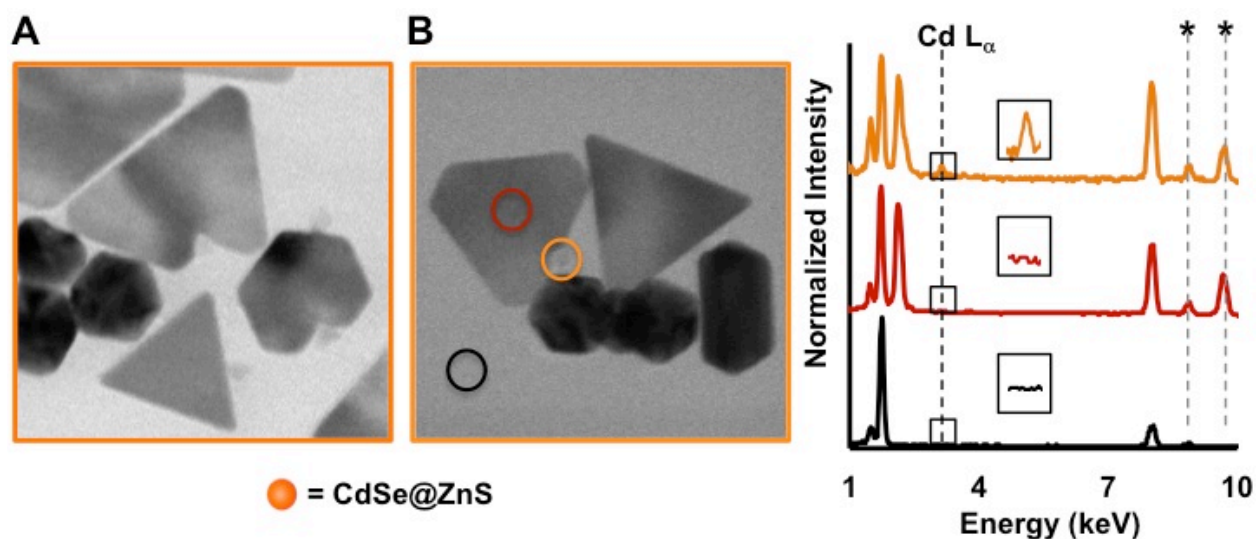


Figure 4.6. Gold nanoprism synthesis performed with CdSe@ZnS quantum dots. (A) Representative image of the prism and spherical impurity products formed. (B) EDX analysis of the products over selected regions colored by circles. The region where the cadmium L_{α} peak should be is boxed and enlarged for clarity. Two characteristic gold peaks are represented by asterisks. Scale bars represent 100nm.

4.3.3 Prism Synthesis with Palladium Nanoparticles Reveals that the Nanoparticle Precursor Templates the Spherical Impurity Products

With strong evidence in support of the homogeneous nucleation of prisms, a compositionally distinct precursor closely mimicking the one used in the original prism synthesis was next used to track the fate of the particle precursor.¹²² In particular, a large palladium particle was chosen, because palladium has a similar crystal structure to gold, and the particle can be easily identified in the product distribution (Figure 4.7).⁹⁵

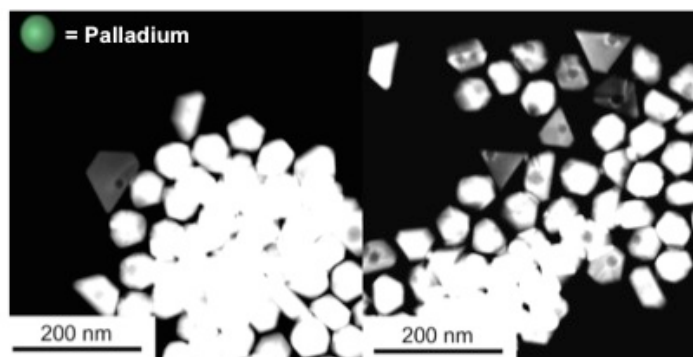


Figure 4.7. Representative image of the gold nanoprism and spherical impurity products formed with palladium nanoparticle precursors.

Interestingly, the prisms synthesized with palladium particle precursors had circular and concave edge features similar to those synthesized with QDs. SEM revealed that these features were holes and EDX identified that in most cases palladium was absent from these holes (Figure 4.8). Conversely, while little palladium was found in the prisms, palladium formed the core of most pseudo-spherical impurity products.

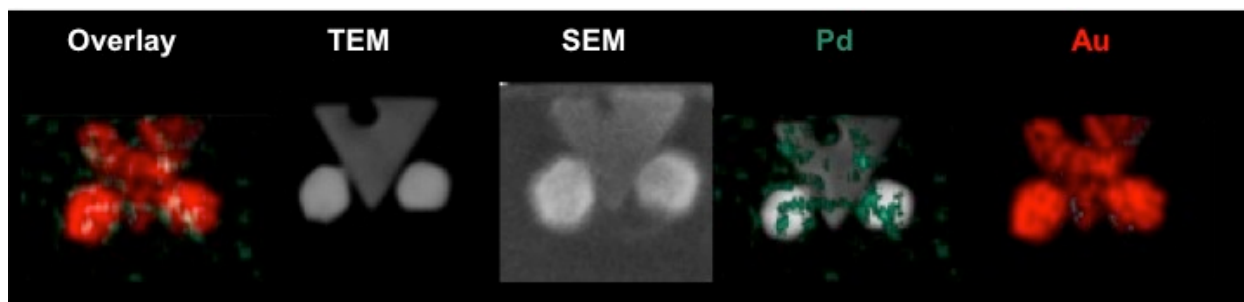


Figure 4.8. EDX analysis of prisms grown from palladium nanoparticle precursors. From left to right, images show a compositional overlay of gold and palladium onto the TEM image, a TEM image, an SEM image, a compositional overlay of palladium onto the TEM image, and a compositional overlay of gold onto the TEM image.

4.3.4 The Nanoparticle Precursor Plays a Dual Catalytic and Templating Role in the Synthesis of Gold Triangular Nanoprisms

The presence of hole features and the absence of palladium and cadmium in the prisms suggest a similar nanoparticle-mediated homogeneous nucleation pathway for both the palladium and QD nanoparticle precursors. Closer inspection of the hole sizes found in the prisms, demonstrate that these holes are of similar size to the initial nanoparticle precursors (Figure 4.9).

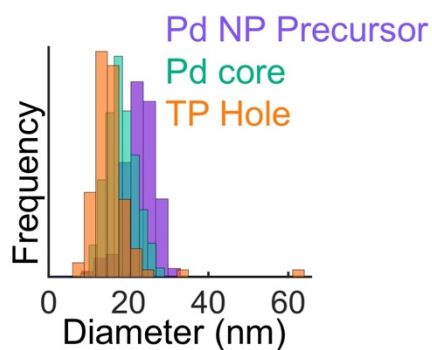


Figure 4.9. Histogram of the size distribution of the initial palladium nanoparticle precursors, the palladium core in the pseudospherical impurity products, and the holes found in resultant prisms.

This finding imply that the prisms form in proximity to the nanoparticle precursors.

Since homogeneous nucleation of gold nanoparticle products requires the reduction of an aqueous gold species, nucleation of prisms near the surface of the palladium and QD particles suggests that nanoparticle precursors can function as catalysts for nucleation through either the direct channeling of an electron to Au^+ or the stabilization of small molecule reducing agents (ascorbate/ascorbyl radical) which promotes reduction of Au^+ (Figure 4.10, path 1). Additionally, the presence of palladium at the core of the impurity particles implies that the nanoparticle precursors may also induce heterogeneous nucleation, in agreement with seed-mediated particle

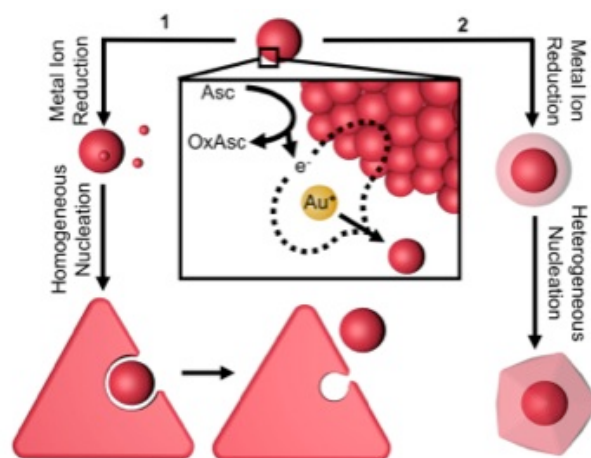


Figure 4.10. Proposed mechanism for the alternate role of the nanoparticle precursors. Path 1: The precursor stabilizes the reducing species (Asc: ascorbate or ascorbyl radical, OxAsc: ascorbyl radical or dehydroascorbic acid) such that it can donate electrons to reduce Au^+ to Au^0 and produce gold nuclei. Path 2: The precursor acts as a template for metal reduction and subsequent growth of pseudospherical impurity particles (e.g. acts as a seed).
synthesis literature (Figure 4.10, path 2).^{123–125}

In both paths 1 and 2, ascorbic acid is identified as the predominant electron source based on reaction stoichiometry, the amount of electrons required for the reduction of gold, and most importantly the final pH of the reaction. Reaction pH was used a proxy for the protonation state of ascorbic acid, which loses two protons upon complete oxidation to dehydroascorbic acid.

Changes in pH were monitored from the initial addition of nanoparticle precursors ($t = 0$) through 90 minutes after addition. The final pH of the reaction (3.1 ± 0.1) indicates that ~ 1.5 protons per ascorbic acid molecule end up in solution. Since two molar equivalents of ascorbic acid are added per HAuCl_4 , ascorbic acid provides enough electrons to reduce Au^{3+} completely to Au^0 .

Lastly, in this synthesis, it is evident that a nanoparticle precursor must also be present in order for nucleation to occur. Interestingly, while a variety of nanoparticle precursor compositions have been shown to catalyze this reaction, there are exceptions. For example, ~ 20 nm TiO_2 precursors did not catalyze the nucleation of prisms (Figure 4.11). This suggests that the interactions between the particle precursor and the molecular species in solution, such as ascorbic acid, are significant and that the presence of a nanoscale surface alone is not sufficient for catalysis. Cumulatively, these data suggest that the same particle population may be both structurally (Figure 4.10, path **2**) and catalytically (Figure 4.10, path **1**) relevant for product nucleation.

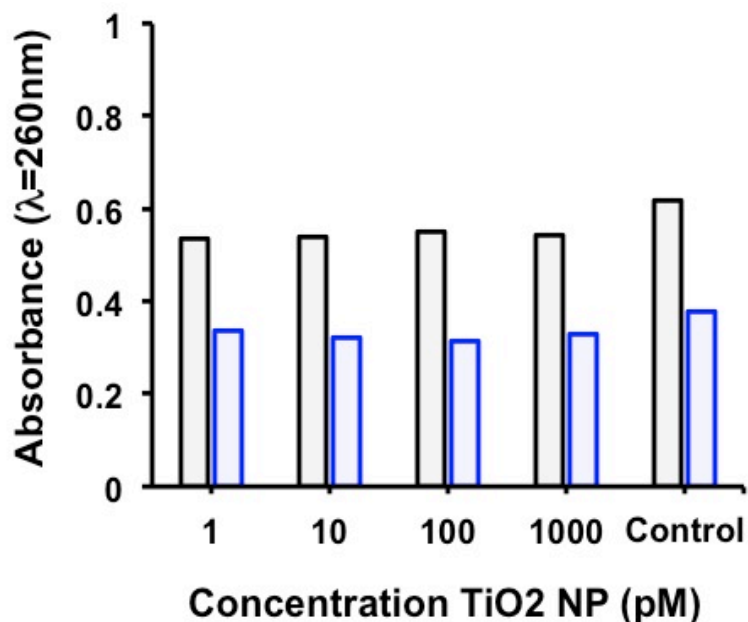


Figure 4.11. Prism growth solutions with TiO₂ (21 nm) nanoparticle precursors show comparable changes in absorption (260 nm) over a 24-hour period to a control growth solution with no nanoparticle precursor added. Black bars indicate the initial absorption for each growth solution. Blue bars show absorption after 24 hours.

4.3.5 Nanoparticle Shape is Used as a Handle to Test and Confirm the Mechanism of Gold

Nanoprism Nucleation

In order to test the proposed mechanism for a gold particle precursor system, we hypothesized that the growth of gold triangular prisms could be prevented or promoted by varying reaction conditions to favor either heterogeneous or homogeneous nucleation, respectively. Homogeneous nucleation was favored by providing fewer sites for heterogeneous nucleation (e.g. reduce particle precursors or “seed” concentration) or by increasing the pH of the reaction (e.g. increase strength of the reducing agent).¹²⁶ Here, particle precursor shape was used as a probe. Under high concentrations of gold single-crystalline nanorod precursors (aspect ratio

($= 3.6 \pm 0.7$) and low pH (pH = 3.4) conditions, heterogeneous nucleation was favored and, in support of the proposed mechanism, prisms were not observed as products (Figure 4.12A). Further, many impurity products with an aspect ratio greater than one were observed, in support of path 2 (Figure 4.10). However, as the gold nanorod concentration decreased or the pH increased, prisms appeared as products (Figure 4.12B). These observations, in addition to the fact that every catalytic particle precursor studied produces the same prism products, suggest that

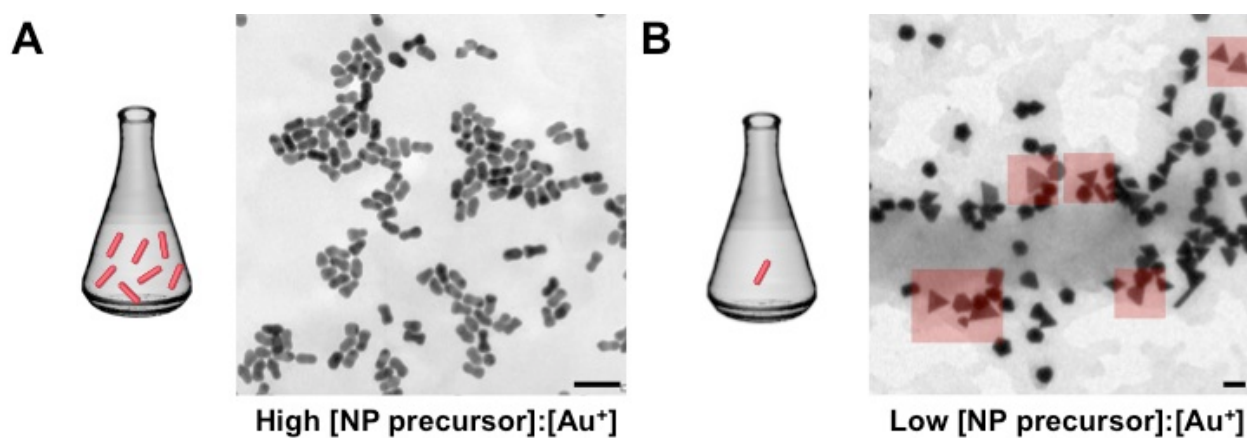


Figure 4.12. Prism growth solutions with gold nanorods as precursors. (A) At high precursor concentrations, heterogeneous nucleation is favored such that prisms are not observed and only anisotropic impurity products are present. (B) At low precursor concentrations, homogeneous nucleation is more prevalent and prisms are observed. Scale bars represent 200nm.

nucleation of prisms likely occurs by the same nanoparticle-catalyzed mechanism with the original gold nanoparticle precursors.

4.4 Conclusions

Cumulatively, this work points toward an alternative role by which nanoparticle precursors can mediate particle synthesis. With respect to the prism synthesis, the ability to produce the same structure, gold triangular prisms, from nanoparticle precursors of diverse size, defect structure, and composition strongly suggests a similar underlying homogeneous nucleation

mechanism catalyzed by the nanoparticle precursor. More broadly, this work highlights that the role of the nanoparticle precursor is reaction dependent. For example, a precursor's catalytic role may explain the distribution of product defect structures associated with some classes of "seed-mediated" syntheses, which often include shape-directing additives (e.g. Ag^+ , I^-). This observation suggests that shape-directing additives in the growth solution may not only direct the product morphology, but also the product nucleation pathway. Ultimately, while improving the uniformity of the seed often leads to improved uniformity in products, the chemical environment and nature of the particle precursor also play significant, and in some cases dominant, roles in dictating both the uniformity and shape of the resultant products.

4.5 Experimental Methods

4.5.1 Prism Growth Solution Preparation

Gold triangular nanoprisms were synthesized according to a literature procedure with modifications.⁶¹ Briefly, 9 mL of 50 mM cetyltrimethylammonium bromide (CTAB) was brought to 50 μM sodium iodide. To this 250 μL of 0.01M chloroauric acid, 50 μL of 0.1M fresh sodium hydroxide and 50 μL of 0.1M fresh ascorbic acid was added. This was defined as the growth solution for each experimental condition. Next this solution was brought to a set concentration of nanoparticle precursor. Concentrations ranged from 5 to 500 pM for the synthesis of prisms with gold multiply-twinned, gold single-crystalline, QDs, and palladium single crystalline nanoparticles. For TiO_2 nanoparticle experiments, concentrations ranged from 1 to 1000 pM. For low particle concentration experiments with single-crystalline gold spheres and rods, concentrations ranged from 0.1 pM to 1 pM. All glassware was rinsed with aqua regia prior to use.

4.5.2 Nanoparticle Precursor Concentration Determination

Gold particle concentration was determined through a UV-Vis spectroscopy measurement in combination with the Beer-Lambert Law. An extinction coefficient was calculated based on particle size, shape and composition. For spherical particles the extinction coefficient can be calculated analytically based on Mie Theory. In order to determine the size of the particles, algorithmic analysis of electron microscopy images of at least 100 nanoparticles was performed.¹¹⁶ ICP-MS was used to determine the concentration of palladium nanoparticles. QD nanoparticle concentrations were given by the manufacturer. A known mass of TiO₂ particles was first suspended in 50 mM CTAB to produce a concentrated stock solution for subsequent experiments.

4.5.3 Nanoparticle Synthesis

Single crystalline, gold spherical particles⁹⁷ and gold rods¹²⁷ were synthesized according to literature protocol. Single-crystalline palladium cubes were synthesized according to a literature protocol.⁹⁵ Immediately after synthesis, the ~22 nm palladium cubes were centrifuged (30 minutes, 15,000 rpm) and resuspended in 50mM CTAB. This process was repeated two times. Aliquots of particles (0.5 mL) were exposed to a range of aqua regia dilutions (2,000 to 20,000x dilution) at 85°C for one hour in order to oxidatively etch the cube corners and form spheres. After an hour of etching, test batches were evaluated with electron microscopy to determine which produced the most uniform, spherical palladium particles. The full batch was subsequently exposed to the same dissolution conditions to produce a uniform batch of single-crystalline spherical palladium nanoparticles. All glassware was rinsed with aqua regia prior to use. The resulting particle products from the above syntheses were characterized by electron microscopy

(Hitachi H8100 200keV, Hitachi HD-2300 200keV) using algorithmic analysis, UV-Vis spectroscopy (Agilent Cary 5000), atomic force microscopy (Bruker Dimension Icon), selected area electron diffraction (SAED) and energy-dispersive x-ray (EDX) spectroscopy.

4.5.4 TEM Sample Preparation

Typically, an aliquot of sample (prism products or particle precursors) was diluted to 1.5 mL with nanopure water in a 1.5 mL Eppendorf centrifuge tube, centrifuged (10 minutes at 10,000 rpm for prism products, 20 minutes at 15,000 rpm for particle precursors unless otherwise noted), and resuspended in nanopure water to approximately four times the volume of the original aliquot. A small volume (1 μL) of a dilute solution (1 μL in 1 mL) of thiolated oligoethyleneglycol (OEG) was added to 9 μL of the above diluted particle solution to a final volume of 10 μL . This volume was deposited on a copper TEM grid. For EDX studies OEG was omitted.

4.5.5 pH Measurement

All pH measurements were carried out using a Mettler Toledo FiveEasy pH meter. The meter was washed three times with nanopure water before each measurement.

CHAPTER 5: Conclusions and Future Directions

5.1 Conclusions

Spherical nucleic acids (SNAs) are a class of DNA-nanoparticle conjugates composed of nanoparticle cores densely functionalized with radially oriented linear DNA. Because of the DNA architecture, these constructs readily enter cells, are highly resistant to nuclease degradation and can bind complementary DNA with binding constants orders of magnitude larger than their linear counterparts. These distinctive properties have enabled the use of SNAs in a variety of applications including gene knockdown, mRNA detection intracellularly and colloidal crystal engineering. The ability of SNAs to bind complementary DNA with orders of magnitude higher affinity is the unifying property for all of these applications. Yet, little was known about the origin of this enhancement and how it could be modified with SNA architecture (i.e. nanoparticle shape and DNA density).

The work detailed here investigates a few of the fundamental factors that govern the effect of architecture on the ability of SNAs to bind complementary DNA. In Chapter 2, the origin of binding enhancement on DNA-functionalized spherical nanoparticles is explained. This work demonstrates that binding to DNA-functionalized nanoparticles is enthalpically enhanced and can be readily tuned by changing the DNA density and distance from the surface. Chapter 3 explores the role of density and nanoparticle curvature on the thermodynamic efficiency of DNA displacement reactions, which govern the efficacy of intracellular mRNA detection probes. Finally, in Chapter 4, the synthesis of highly anisotropic gold triangular prisms is found to be governed by a homogeneous nucleation mechanism, a discovery that explains low product yield and shifts the focus of improving yield to reaction conditions that favor homogeneous nucleation. These studies delineate how the architecture of DNA functionalized nanoparticles can be

modified to better favor the hybridization of a complementary nucleic acid target, and suggest strategies for moving beyond the spherical architecture into more anisotropic shapes.

5.2 Future Directions

5.2.1 The Electron Donating Role of the Nanoparticle Precursor in the Synthesis of Gold

Triangular Prisms

The synthesis of anisotropic noble metal nanoparticles has been made possible by advancements in seed-mediated synthesis, whereby separation of product nucleation from growth helps control uniformity and yield. This synthetic strategy relies on the ability to promote heterogeneous nucleation by introducing a preformed nanoparticle precursor into a metal cation reaction solution. This suggests that the uniformity of the nanoparticle precursor can dictate the uniformity of products. Efforts toward improving nanoparticle precursor uniformity in order to increase product uniformity have therefore been met with great success. Interestingly, there are nanoparticle shapes for which this heterogeneous nucleation principle breaks down. In the synthesis of gold triangular nanoprisms, prism formation proceeds via a nanoparticle precursor catalyzed homogeneous nucleation mechanism. In this case, the chemical and structural identity of the seed has been shown to matter very little. This finding suggests that to improve product uniformity and yield for certain anisotropic nanoparticle shapes, the focus should be placed on finding reaction conditions that promote homogeneous nucleation. The sum of these observations raises some questions about what specific role the catalytic nanoparticle precursor plays in promoting homogeneous nucleation.

Preliminary data suggests that the catalytic nanoparticle precursor behaves as an electron shuttle in the synthesis of gold triangular nanoprisms. One of the nanoparticle precursors used to demonstrate that the prism synthesis does not proceed by a heterogeneous nucleation mechanism was a core-shell CdSe@ZnS quantum dot (QD). QDs proved to be excellent substitutes for the original gold nanoparticle precursors, because just like the gold precursors they generate prisms

in equal yields and enable prism edge length to be tuned with simple changes in their concentration. To further probe the capabilities of QDs as precursors, the role of photoexcitation was tested. Light-induced carrier separation in QDs has been shown previously to promote heterogeneous nucleation of gold,^{120,128} so I hypothesized that exposure of the prism synthesis to light of specific wavelengths would have interesting repercussions for the product distribution. Specifically, a wavelength energetic enough to photoexcite the QD precursors would activate the carrier donating abilities of the QDs while a lower energy light would suppress electron donation. The CdSe@ZnS QDs have a first exciton maximum wavelength of 593nm. In this experiment the QD concentration was held constant, while the growth solution was exposed to different wavelengths of light 550nm, 750nm light, and ambient light as a control. The prism edge length can be tuned by the wavelength of light to which the growth solution is exposed (Figure 5.1). When light that is more energetic than the first exciton (550nm) is used, prism edge length is smaller, which suggest more homogenous nucleation events occur. Conversely when the wavelength of light is less energetic (750nm) prism edge length is larger than that of prisms synthesized under ambient light. This can be seen in both the electron microscopy images (Figure 5.1B) as well as the UV-Vis spectroscopy data (Figure 5.1C). These observations imply that the ability of the nanoparticle precursor to receive and donate electrons is important for promoting homogenous nucleation. They further suggest that the nanoparticle precursor has a role in reducing gold, either as the reducing agent or a shuttle of electrons. Studies to understand how homogenous nucleation depends on the electron donating ability of the nanoparticle precursor should be undertaken.

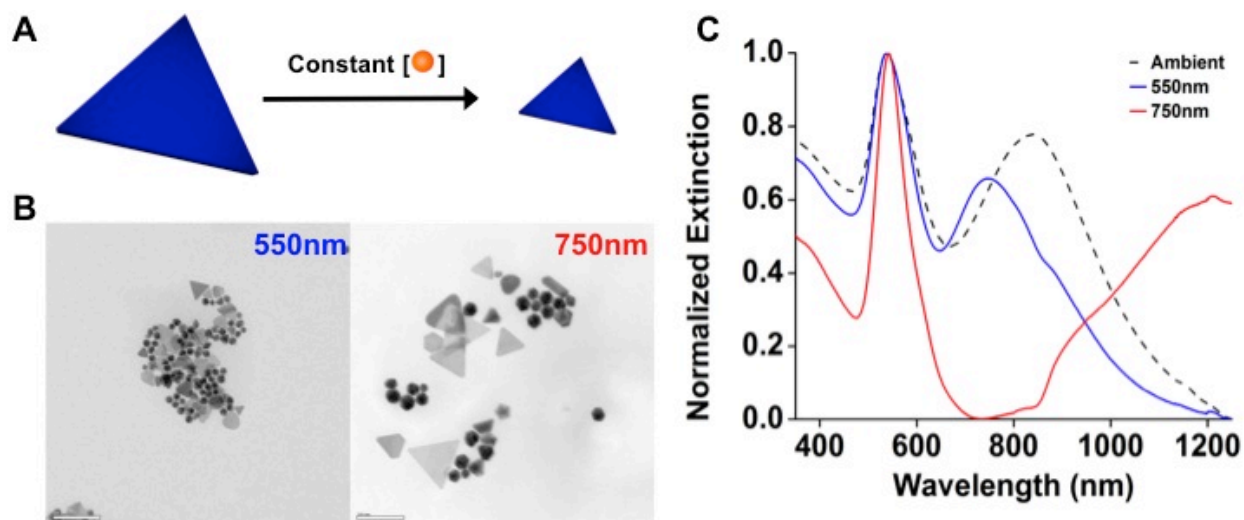


Figure 5.1. (A) Depiction of the effect of exposure of different wavelengths of light on the prism edge length with constant quantum dot precursor concentration. (B) TEM images of prisms synthesized with 550nm and 750nm light (scale bars are 200nm). (C) UV-Vis data of prisms synthesized with 550nm, 750nm and ambient light. The red shift in the near infrared resonance peak describes an increase in the prism edge length.

Cyclic voltammetry can be used to track the electrons in the system, and justify the need for a nanoparticle precursor. This study could provide insight into how the nanoparticle precursor can be designed or substituted to more effectively promote homogenous nucleation and increase the yield of triangular prisms.

5.2.2 The Salt Dependence of DNA Hybridization on DNA Functionalized Nanoparticle

Surfaces

Spherical nucleic acids (SNAs), constructs composed of nanoparticles densely functionalized with linear DNA, are promising constructs for intracellular gene regulation and detection. Their therapeutic efficacy is highly dependent on how the thermodynamics of DNA hybridization are modified on the surface. Therefore, understanding the fundamental forces that drive hybridization onto SNAs will inform the development of better therapeutics and diagnostics. At a molecular level, these constructs offer a promising platform for understanding

the thermodynamic consequences of confining DNA hybridization to surfaces. Electrostatic and steric hindrance due to surface confinement should play a significant role in the thermodynamics of hybridization to DNA-functionalized surfaces. The salt dependence of hybridization to SNAs could help elucidate the contributions from electrostatics and sterics, especially in comparison to linear DNA hybridization.

Preliminary experiments using a van' t Hoff analysis were performed to determine the thermodynamics of hybridization on SNAs and linear DNA. These experiments show that the enthalpy of DNA hybridization on SNAs becomes more negative (more favorable) with increasing salt concentration, but precipitously increases (becomes less favorable) at 1M salt (Figure 5.2). This is in contrast to linear DNA for which enthalpy remains constant, within error, with increasing salt. These data suggest that at high salt concentrations, electrostatic screening of surface-bound DNA is no longer the dominant role of salt in solution. Additionally, these enthalpic changes are accompanied by equal and opposite changes in the entropy of hybridization, such that the free energy of DNA hybridization on SNAs remains constant with increasing salt. The effect of high salt on the hybridization of linear DNA to SNAs should be

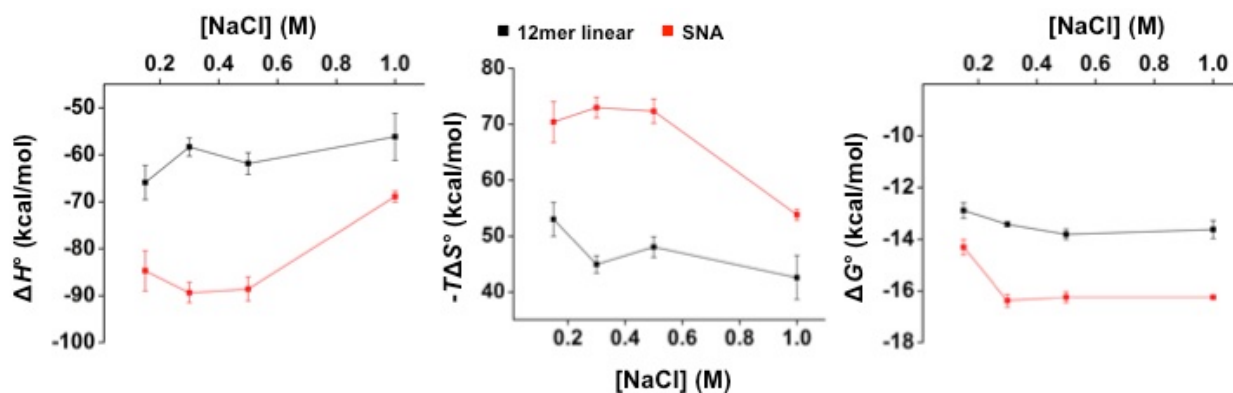


Figure 5.2. The salt dependence of the enthalpy, entropy and free energy of hybridization for 12mer linear DNA (black) and spherical nucleic acids (red) of comparable sequence.

explored, as it can greatly influence the implementation of SNAs in *in vitro* detection and crystal engineering applications.

5.2.3 The Mechanism of DNA Melting from DNA-Functionalized Nanoparticles

DNA-functionalized gold nanoparticles (DNA-AuNPs) experimentally exhibit an enhanced binding affinity for complementary DNA, compared to free DNA systems. Understanding this effect is important for the design of DNA-AuNPs for diagnostic and therapeutic applications, because their mechanism of action depends on the energetics of duplex hybridization onto the surface. A mechanistic description of this phenomenon is lacking. All-atom, explicit solvent simulations provide the most realistic description of DNA structure and dynamics, but the time scales necessary to capture DNA melting have previously been computationally prohibitive for systems of this size and complexity.

Preliminary experiments use atomistic molecular dynamics simulations to determine the melting mechanism of a 9mer-DNA duplex that is chemically bonded to a nanoparticle surface and compare it to the mechanism of a linear 9mer-DNA duplex (Figure 5.3). These experiments

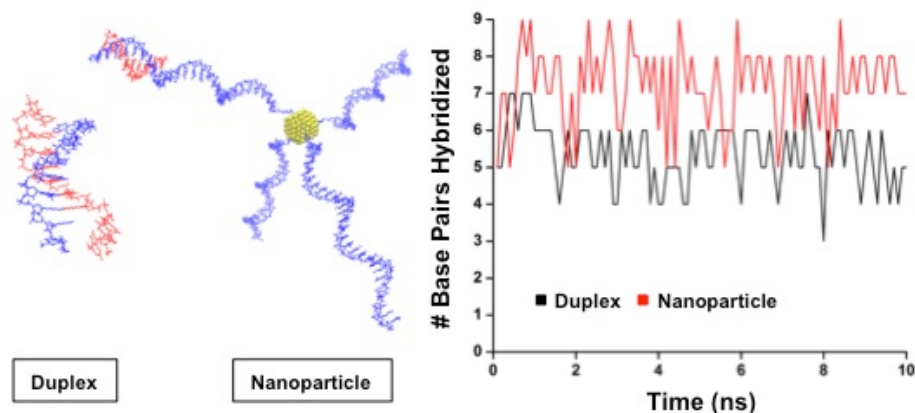


Figure 5.3. Atomistic molecular dynamics simulations demonstrating the first 10ns of melting for a linear duplex and a nanoparticle-bound duplex. The number of base pairs hybridized is plotted as a function of time as a measure of stability.

show that even within the first few nanoseconds of simulation, the linear DNA duplex is more destabilized than the nanoparticle bound duplex. Stability is determined by measuring the number of hybridized DNA base-pairs as a function of time. The linear DNA duplex has five to six base-pairs on average, while the nanoparticle-bound duplex has seven to eight. This suggests that melting from the nanoparticle occurs by a different mechanism than melting free in solution. A deeper understanding of this mechanism could help with predictions of thermodynamic constants for hybridization onto DNA-functionalized nanoparticles.

REFERENCES

1. Mirkin, C. A., Letsinger, R. L., Mucic, R. C. & Storhoff, J. J. A DNA-based method for rationally assembling nanoparticles into macroscopic materials. *Nature* **382**, 607–609 (1996).
2. Cutler, J. I., Auyeung, E. & Mirkin, C. A. Spherical nucleic acids. *J. Am. Chem. Soc.* **134**, 1376–1391 (2012).
3. Hurst, S. J., Lytton-Jean, A. K. R. & Mirkin, C. A. Maximizing DNA Loading on a Range of Gold Nanoparticle Sizes. *Anal. Chem.* **78**, 8313–8318 (2006).
4. Hill, H. D., Millstone, J. E., Banholzer, M. J. & Mirkin, C. A. The Role Radius of Curvature Plays in Thiolated Oligonucleotide Loading on Gold Nanoparticles. *ACS Nano* **3**, 418–424 (2009).
5. Cutler, J. I. *et al.* Polyvalent Nucleic Acid Nanostructures. *J. Am. Chem. Soc.* **133**, 9254–9257 (2011).
6. Zhang, C. *et al.* Biodegradable DNA-Brush Block Copolymer Spherical Nucleic Acids Enable Transfection Agent-Free Intracellular Gene Regulation. *Small* **11**, 5360–5368
7. Banga, R. J., Chernyak, N., Narayan, S. P., Nguyen, S. T. & Mirkin, C. A. Liposomal Spherical Nucleic Acids. *J. Am. Chem. Soc.* **136**, 9866–9869 (2014).
8. Tan, X. *et al.* Blurring the Role of Oligonucleotides: Spherical Nucleic Acids as a Drug Delivery Vehicle. *J. Am. Chem. Soc.* **138**, 10834–10837 (2016).
9. Young, K. L. *et al.* Hollow Spherical Nucleic Acids for Intracellular Gene Regulation Based upon Biocompatible Silica Shells. *Nano Lett.* **12**, 3867–3871 (2012).
10. Rische, C. H., Goel, A., Radovic-Moreno, A. F. & Gryaznov, S. M. Antibacterial silver core spherical nucleic acids. *Mater. Today Commun.* **9**, 30–40 (2016).

11. Lee, J.-S., Lytton-Jean, A. K. R., Hurst, S. J. & Mirkin, C. A. Silver Nanoparticle–Oligonucleotide Conjugates Based on DNA with Triple Cyclic Disulfide Moieties. *Nano Lett.* **7**, 2112–2115 (2007).
12. Calabrese, C. M. *et al.* Biocompatible Infinite-Coordination-Polymer Nanoparticle–Nucleic-Acid Conjugates for Antisense Gene Regulation. *Angew. Chem. Int. Ed.* **54**, 476–480
13. Morris, W., Briley, W. E., Auyeung, E., Cabezas, M. D. & Mirkin, C. A. Nucleic Acid–Metal Organic Framework (MOF) Nanoparticle Conjugates. *J. Am. Chem. Soc.* **136**, 7261–7264 (2014).
14. Cutler, J. I., Zheng, D., Xu, X., Giljohann, D. A. & Mirkin, C. A. Polyvalent Oligonucleotide Iron Oxide Nanoparticle “Click” Conjugates. *Nano Lett.* **10**, 1477–1480 (2010).
15. Brodin, J. D., Sprangers, A. J., McMillan, J. R. & Mirkin, C. A. DNA-Mediated Cellular Delivery of Functional Enzymes. *J. Am. Chem. Soc.* **137**, 14838–14841 (2015).
16. Rosi, N. L. *et al.* Oligonucleotide-Modified Gold Nanoparticles for Intracellular Gene Regulation. *Science* **312**, 1027–1030 (2006).
17. Choi, C. H. J., Hao, L., Narayan, S. P., Auyeung, E. & Mirkin, C. A. Mechanism for the endocytosis of spherical nucleic acid nanoparticle conjugates. *Proc. Natl. Acad. Sci.* **110**, 7625–7630 (2013).
18. Giljohann, D. A. *et al.* Oligonucleotide Loading Determines Cellular Uptake of DNA-Modified Gold Nanoparticles. *Nano Lett.* **7**, 3818–3821 (2007).
19. Chul Song, W., Kim, K.-R., Park, M., Eun Lee, K. & Ahn, D.-R. Backbone-modified oligonucleotides for tuning the cellular uptake behaviour of spherical nucleic acids. *Biomater. Sci.* **5**, 412–416 (2017).

20. Narayan, S. P. *et al.* The Sequence-Specific Cellular Uptake of Spherical Nucleic Acid Nanoparticle Conjugates. *Small* **11**, 4173–4182
21. Seferos, D. S., Prigodich, A. E., Giljohann, D. A., Patel, P. C. & Mirkin, C. A. Polyvalent DNA Nanoparticle Conjugates Stabilize Nucleic Acids. *Nano Lett.* **9**, 308–311 (2009).
22. Kewalramani, S. *et al.* Counterion Distribution Surrounding Spherical Nucleic Acid–Au Nanoparticle Conjugates Probed by Small-Angle X-ray Scattering. *ACS Nano* **7**, 11301–11309 (2013).
23. Lytton-Jean, A. K. R. & Mirkin, C. A. A thermodynamic investigation into the binding properties of DNA functionalized gold nanoparticle probes and molecular fluorophore probes. *J. Am. Chem. Soc.* **127**, 12754–12755 (2005).
24. Randeria, P. S. *et al.* What Controls the Hybridization Thermodynamics of Spherical Nucleic Acids? *J. Am. Chem. Soc.* **137**, 3486–3489 (2015).
25. Morrison, L. E. & Stols, L. M. Sensitive fluorescence-based thermodynamic and kinetic measurements of DNA hybridization in solution. *Biochemistry (Mosc.)* **32**, 3095–3104 (1993).
26. Marky, L. A. & Breslauer, K. J. Calculating thermodynamic data for transitions of any molecularity from equilibrium melting curves. *Biopolymers* **26**, 1601–1620 (1987).
27. SantaLucia, J. A unified view of polymer, dumbbell, and oligonucleotide DNA nearest-neighbor thermodynamics. *Proc. Natl. Acad. Sci.* **95**, 1460–1465 (1998).
28. Zheng, D. *et al.* Topical delivery of siRNA-based spherical nucleic acid nanoparticle conjugates for gene regulation. *Proc. Natl. Acad. Sci.* **109**, 11975–11980 (2012).
29. Randeria, P. S. *et al.* siRNA-based spherical nucleic acids reverse impaired wound healing in diabetic mice by ganglioside GM3 synthase knockdown. *Proc. Natl. Acad. Sci.* **112**, 5573–5578 (2015).

30. Jensen, S. A. *et al.* Spherical Nucleic Acid Nanoparticle Conjugates as an RNAi-Based Therapy for Glioblastoma. *Sci. Transl. Med.* **5**, 209ra152-209ra152 (2013).
31. Clancy, S. RNA Functions. *Nat. Educ.* **1**, 102 (2008).
32. Brown, P. O. & Botstein, D. Exploring the new world of the genome with DNA microarrays. *Nat. Genet.* **21**, 33–37 (1999).
33. Sassolas, A., Leca-Bouvier, B. D. & Blum, L. J. DNA Biosensors and Microarrays. *Chem. Rev.* **108**, 109–139 (2008).
34. Ravan, H., Kashanian, S., Sanadgol, N., Badoei-Dalfard, A. & Karami, Z. Strategies for optimizing DNA hybridization on surfaces. *Anal. Biochem.* **444**, 41–46 (2014).
35. Querido, E. & Chartrand, P. Using Fluorescent Proteins to Study mRNA Trafficking in Living Cells. in *Methods in Cell Biology* **85**, 273–292 (Academic Press, 2008).
36. Dirks, R. & Tanke, H. Advances in fluorescent tracking of nucleic acids in living cell. *BioTechniques* **40**, 489–496 (2006).
37. Rodriguez, A. J., Condeelis, J., Singer, R. H. & Dictenberg, J. B. Imaging mRNA movement from transcription sites to translation sites. *Semin. Cell Dev. Biol.* **18**, 202–208 (2007).
38. Kaufmann, B. B. & van Oudenaarden, A. Stochastic gene expression: from single molecules to the proteome. *Curr. Opin. Genet. Dev.* **17**, 107–112 (2007).
39. Prigodich, A. E. *et al.* Multiplexed nanoflares: mRNA detection in live cells. *Anal. Chem.* **84**, 2062–2066 (2012).
40. Prigodich, A. E. *et al.* Nano-flares for mRNA regulation and detection. *ACS Nano* **3**, 2147–2152 (2009).

41. Seferos, D. S., Giljohann, D. A., Hill, H. D., Prigodich, A. E. & Mirkin, C. A. Nano-flares: probes for transfection and mRNA detection in living cells. *J. Am. Chem. Soc.* **129**, 15477–15479 (2007).
42. Dubertret, B., Calame, M. & Libchaber, A. J. Single-mismatch detection using gold-quenched fluorescent oligonucleotides. *Nat. Biotechnol.* **19**, 365–370 (2001).
43. Park, S. Y. *et al.* DNA-programmable nanoparticle crystallization. *Nature* **451**, 553–556 (2008).
44. Nykypanchuk, D., Maye, M. M., van der Lelie, D. & Gang, O. DNA-guided crystallization of colloidal nanoparticles. *Nature* **451**, 549–552 (2008).
45. Macfarlane, R. J. *et al.* Nanoparticle Superlattice Engineering with DNA. *Science* **334**, 204–208 (2011).
46. Macfarlane, R. J., Jones, M. R., Lee, B., Auyeung, E. & Mirkin, C. A. Topotactic Interconversion of Nanoparticle Superlattices. *Science* **341**, 1222–1225 (2013).
47. Kim, Y., Macfarlane, R. J., Jones, M. R. & Mirkin, C. A. Transmutable nanoparticles with reconfigurable surface ligands. *Science* **351**, 579–582 (2016).
48. Auyeung, E. *et al.* DNA-mediated nanoparticle crystallization into Wulff polyhedra. *Nature* **505**, 73–77 (2014).
49. Macfarlane, R. J. *et al.* Establishing the Design Rules for DNA-Mediated Programmable Colloidal Crystallization. *Angew. Chem.* **122**, 4693–4696
50. Zhang, C. *et al.* A general approach to DNA-programmable atom equivalents. *Nat. Mater.* **12**, 741–746 (2013).

51. Kim, Y., Macfarlane, R. J. & Mirkin, C. A. Dynamically Interchangeable Nanoparticle Superlattices Through the Use of Nucleic Acid-Based Allosteric Effectors. *J. Am. Chem. Soc.* **135**, 10342–10345 (2013).
52. Auyeung, E., Macfarlane, R. J., Choi, C. H. J., Cutler, J. I. & Mirkin, C. A. Transitioning DNA-Engineered Nanoparticle Superlattices from Solution to the Solid State. *Adv. Mater.* **24**, 5181–5186
53. Park, D. J. *et al.* Plasmonic photonic crystals realized through DNA-programmable assembly. *Proc. Natl. Acad. Sci.* **112**, 977–981 (2015).
54. Young, K. L. *et al.* Using DNA to Design Plasmonic Metamaterials with Tunable Optical Properties. *Adv. Mater.* **26**, 653–659
55. Ross, M. B., Ku, J. C., Vaccarezza, V. M., Schatz, G. C. & Mirkin, C. A. Nanoscale form dictates mesoscale function in plasmonic DNA–nanoparticle superlattices. *Nat. Nanotechnol.* **10**, 453–458 (2015).
56. Wong, I. Y. & Melosh, N. A. Directed hybridization and melting of DNA linkers using counterion-screened electric fields. *Nano Lett.* **9**, 3521–3526 (2009).
57. Wong, I. Y. & Melosh, N. A. An electrostatic model for DNA surface hybridization. *Biophys. J.* **98**, 2954–2963 (2010).
58. Irving, D., Gong, P. & Levicky, R. DNA surface hybridization: comparison of theory and experiment. *J. Phys. Chem. B* **114**, 7631–7640 (2010).
59. Xu, J. & Craig, S. L. Thermodynamics of DNA hybridization on gold nanoparticles. *J. Am. Chem. Soc.* **127**, 13227–13231 (2005).
60. Chen, C., Wang, W., Ge, J. & Zhao, X. S. Kinetics and thermodynamics of DNA hybridization on gold nanoparticles. *Nucleic Acids Res.* **37**, 3756–3765 (2009).

61. Jones, M. R. & Mirkin, C. A. Bypassing the limitations of classical chemical purification with DNA-programmable nanoparticle recrystallization. *Angew. Chem. Int. Ed Engl.* **52**, 2886–2891 (2013).
62. Young, K. L. *et al.* Assembly of reconfigurable one-dimensional colloidal superlattices due to a synergy of fundamental nanoscale forces. *Proc. Natl. Acad. Sci.* **109**, 2240–2245 (2012).
63. Alhasan, A. H. *et al.* Scanometric microRNA array profiling of prostate cancer markers using spherical nucleic acid-gold nanoparticle conjugates. *Anal. Chem.* **84**, 4153–4160 (2012).
64. Taton, T. A., Mirkin, C. A. & Letsinger, R. L. Scanometric DNA array detection with nanoparticle probes. *Science* **289**, 1757–1760 (2000).
65. Briley, W. E., Bondy, M. H., Randeria, P. S., Dupper, T. J. & Mirkin, C. A. Quantification and real-time tracking of RNA in live cells using Sticky-flares. *Proc. Natl. Acad. Sci. U. S. A.* **112**, 9591–9595 (2015).
66. Liu, W. *et al.* Diamond family of nanoparticle superlattices. *Science* **351**, 582–586 (2016).
67. Martinez-Veracoechea, F. J., Mladek, B. M., Tkachenko, A. V. & Frenkel, D. Design Rule for Colloidal Crystals of DNA-Functionalized Particles. *Phys. Rev. Lett.* **107**, 045902 (2011).
68. Angioletti-Uberti, S., Mognetti, B. M. & Frenkel, D. Re-entrant melting as a design principle for DNA-coated colloids. *Nat. Mater.* **11**, 518–522 (2012).
69. Feng Lang, Dreyfus Rémi, Sha Ruojie, Seeman Nadrian C. & Chaikin Paul M. DNA Patchy Particles. *Adv. Mater.* **25**, 2779–2783 (2013).
70. Schmitt, T. J. & Knotts, T. A. Thermodynamics of DNA hybridization on surfaces. *J. Chem. Phys.* **134**, 205105 (2011).

71. Mergny, J.-L. & Lacroix, L. Analysis of thermal melting curves. *Oligonucleotides* **13**, 515–537 (2003).
72. Holbrook, J. A., Capp, M. W., Saecker, R. M. & Record, M. T. Enthalpy and heat capacity changes for formation of an oligomeric DNA duplex: interpretation in terms of coupled processes of formation and association of single-stranded helices. *Biochemistry (Mosc.)* **38**, 8409–8422 (1999).
73. Wu, P., Nakano, S. & Sugimoto, N. Temperature dependence of thermodynamic properties for DNA/DNA and RNA/DNA duplex formation. *Eur. J. Biochem.* **269**, 2821–2830 (2002).
74. Mikulecky, P. J. & Feig, A. L. Heat capacity changes associated with DNA duplex formation: salt- and sequence-dependent effects. *Biochemistry (Mosc.)* **45**, 604–616 (2006).
75. Freire, E., Mayorga, O. L. & Straume, M. Isothermal titration calorimetry. *Anal. Chem.* **62**, 950A-959A (1990).
76. Jelesarov, I. & Bosshard, H. R. Isothermal titration calorimetry and differential scanning calorimetry as complementary tools to investigate the energetics of biomolecular recognition. *J. Mol. Recognit. JMR* **12**, 3–18 (1999).
77. Riccelli, P. V. *et al.* Thermodynamic, Spectroscopic, and Equilibrium Binding Studies of DNA Sequence Context Effects in Six 22-Base Pair Deoxyoligonucleotides. *Biochemistry (Mosc.)* **38**, 11197–11208 (1999).
78. Rouzina, I. & Bloomfield, V. A. Heat Capacity Effects on the Melting of DNA. 1. General Aspects. *Biophys. J.* **77**, 3242–3251 (1999).

79. Jin, R., Wu, G., Li, Z., Mirkin, C. A. & Schatz, G. C. What Controls the Melting Properties of DNA-Linked Gold Nanoparticle Assemblies? *J. Am. Chem. Soc.* **125**, 1643–1654 (2003).
80. Knotts, T. A., Rathore, N., Schwartz, D. C. & de Pablo, J. J. A coarse grain model for DNA. *J. Chem. Phys.* **126**, 084901 (2007).
81. Sambriski, E. J., Schwartz, D. C. & de Pablo, J. J. A mesoscale model of DNA and its renaturation. *Biophys. J.* **96**, 1675–1690 (2009).
82. Hinckley, D. M., Freeman, G. S., Whitmer, J. K. & de Pablo, J. J. An experimentally-informed coarse-grained 3-Site-Per-Nucleotide model of DNA: structure, thermodynamics, and dynamics of hybridization. *J. Chem. Phys.* **139**, 144903 (2013).
83. Lomzov, A. A., Vorobjev, Y. N. & Pyshnyi, D. V. Evaluation of the Gibbs Free Energy Changes and Melting Temperatures of DNA/DNA Duplexes Using Hybridization Enthalpy Calculated by Molecular Dynamics Simulation. *J. Phys. Chem. B* **119**, 15221–15234 (2015).
84. Koshkin, A. A. *et al.* LNA (Locked Nucleic Acids): Synthesis of the adenine, cytosine, guanine, 5-methylcytosine, thymine and uracil bicyclonucleoside monomers, oligomerisation, and unprecedented nucleic acid recognition. *Tetrahedron* **54**, 3607–3630 (1998).
85. Koshkin, A. A. *et al.* LNA (Locked Nucleic Acid): An RNA Mimic Forming Exceedingly Stable LNA:LNA Duplexes. *J. Am. Chem. Soc.* **120**, 13252–13253 (1998).
86. Kaur, H., Wengel, J. & Maiti, S. Thermodynamics of DNA-RNA heteroduplex formation: effects of locked nucleic acid nucleotides incorporated into the DNA strand. *Biochemistry (Mosc.)* **47**, 1218–1227 (2008).

87. Kierzek, E. *et al.* Contributions of stacking, preorganization, and hydrogen bonding to the thermodynamic stability of duplexes between RNA and 2'-O-methyl RNA with locked nucleic acids. *Biochemistry (Mosc.)* **48**, 4377–4387 (2009).
88. Owczarzy, R., You, Y., Groth, C. L. & Tataurov, A. V. Stability and mismatch discrimination of locked nucleic acid-DNA duplexes. *Biochemistry (Mosc.)* **50**, 9352–9367 (2011).
89. Randeria, P. S. *et al.* Nanoflares as Probes for Cancer Diagnostics. in *Nanotechnology-Based Precision Tools for the Detection and Treatment of Cancer* 1–22 (Springer, Cham, 2015). doi:10.1007/978-3-319-16555-4_1
90. Rogers, W. B. & Manoharan, V. N. Programming colloidal phase transitions with DNA strand displacement. *Science* **347**, 639–642 (2015).
91. Zhang, D. Y. & Seelig, G. Dynamic DNA nanotechnology using strand-displacement reactions. *Nat. Chem.* **3**, 103–113 (2011).
92. Turkevich, J., Stevenson, P. C. & Hillier, J. A study of the nucleation and growth processes in the synthesis of colloidal gold. *Discuss. Faraday Soc.* **11**, 55–75 (1951).
93. Burda, C., Chen, X., Narayanan, R. & El-Sayed, M. A. Chemistry and properties of nanocrystals of different shapes. *Chem. Rev.* **105**, 1025–1102 (2005).
94. Xia, Y., Xiong, Y., Lim, B. & Skrabalak, S. E. Shape-controlled synthesis of metal nanocrystals: simple chemistry meets complex physics? *Angew. Chem. Int. Ed Engl.* **48**, 60–103 (2009).
95. Niu, W., Zhang, L. & Xu, G. Shape-controlled synthesis of single-crystalline palladium nanocrystals. *ACS Nano* **4**, 1987–1996 (2010).

96. Lohse, S. E. & Murphy, C. J. The Quest for Shape Control: A History of Gold Nanorod Synthesis. *Chem. Mater.* **25**, 1250–1261 (2013).
97. O'Brien, M. N., Jones, M. R., Brown, K. A. & Mirkin, C. A. Universal noble metal nanoparticle seeds realized through iterative reductive growth and oxidative dissolution reactions. *J. Am. Chem. Soc.* **136**, 7603–7606 (2014).
98. Jana, N. R., Gearheart, L. & Murphy, C. J. Wet Chemical Synthesis of High Aspect Ratio Cylindrical Gold Nanorods. *J. Phys. Chem. B* **105**, 4065–4067 (2001).
99. Liu, M. & Guyot-Sionnest, P. Mechanism of silver(I)-assisted growth of gold nanorods and bipyramids. *J. Phys. Chem. B* **109**, 22192–22200 (2005).
100. Grzelczak, M., Pérez-Juste, J., Mulvaney, P. & Liz-Marzán, L. M. Shape control in gold nanoparticle synthesis. *Chem. Soc. Rev.* **37**, 1783–1791 (2008).
101. O'Brien, M. N., Jones, M. R. & Mirkin, C. A. The nature and implications of uniformity in the hierarchical organization of nanomaterials. *Proc. Natl. Acad. Sci. U. S. A.* **113**, 11717–11725 (2016).
102. Grzelczak, M. *et al.* Silver Ions Direct Twin-Plane Formation during the Overgrowth of Single-Crystal Gold Nanoparticles. *ACS Omega* **1**, 177–181 (2016).
103. Grzelczak, M. *et al.* Influence of Iodide Ions on the Growth of Gold Nanorods: Tuning Tip Curvature and Surface Plasmon Resonance. *Adv. Funct. Mater.* **18**, 3780–3786 (2008).
104. Personick, M. L. *et al.* Synthesis and isolation of {110}-faceted gold bipyramids and rhombic dodecahedra. *J. Am. Chem. Soc.* **133**, 6170–6173 (2011).
105. Millstone, J. E., Métraux, G. S. & Mirkin, C. A. Controlling the Edge Length of Gold Nanoprisms via a Seed-Mediated Approach. *Adv. Funct. Mater.* **16**, 1209–1214 (2006).

106. Ha, T. H., Koo, H.-J. & Chung, B. H. Shape-Controlled Syntheses of Gold Nanoprisms and Nanorods Influenced by Specific Adsorption of Halide Ions. *J. Phys. Chem. C* **111**, 1123–1130 (2007).
107. Lofton, C. & Sigmund, W. Mechanisms Controlling Crystal Habits of Gold and Silver Colloids. *Adv. Funct. Mater.* **15**, 1197–1208 (2005).
108. Jana, N. R., Gearheart, L. & Murphy, C. J. Evidence for Seed-Mediated Nucleation in the Chemical Reduction of Gold Salts to Gold Nanoparticles. *Chem. Mater.* **13**, 2313–2322 (2001).
109. Millstone, J. E., Hurst, S. J., Métraux, G. S., Cutler, J. I. & Mirkin, C. A. Colloidal Gold and Silver Triangular Nanoprisms. *Small* **5**, 646–664 (2009).
110. Duff, D. G. *et al.* The Morphology and Microstructure of Colloidal Silver and Gold. *Angew. Chem. Int. Ed. Engl.* **26**, 676–678 (1987).
111. Malikova, N., Pastoriza-Santos, I., Schierhorn, M., Kotov, N. A. & Liz-Marzán, L. M. Layer-by-Layer Assembled Mixed Spherical and Planar Gold Nanoparticles: Control of Interparticle Interactions. *Langmuir* **18**, 3694–3697 (2002).
112. Shankar, S. S. *et al.* Biological synthesis of triangular gold nanoprisms. *Nat. Mater.* **3**, 482–488 (2004).
113. Shankar, S. S., Bhargava, S. & Sastry, M. Synthesis of gold nanospheres and nanotriangles by the Turkevich approach. *J. Nanosci. Nanotechnol.* **5**, 1721–1727 (2005).
114. Straney, P. J., Marbella, L. E., Andolina, C. M., Nuhfer, N. T. & Millstone, J. E. Decoupling Mechanisms of Platinum Deposition on Colloidal Gold Nanoparticle Substrates. *J. Am. Chem. Soc.* **136**, 7873–7876 (2014).
115. Personick, M. L. & Mirkin, C. A. Making sense of the mayhem behind shape control in the synthesis of gold nanoparticles. *J. Am. Chem. Soc.* **135**, 18238–18247 (2013).

116. Laramy, C. R., Brown, K. A., O'Brien, M. N. & Mirkin, C. A. High-Throughput, Algorithmic Determination of Nanoparticle Structure from Electron Microscopy Images. *ACS Nano* **9**, 12488–12495 (2015).
117. Alivisatos, A. P. Perspectives on the Physical Chemistry of Semiconductor Nanocrystals. *J. Phys. Chem.* **100**, 13226–13239 (1996).
118. Ajayan, P. M. & Marks, L. D. Phase instabilities in small particles. *Phase Transit.* **24–26**, 229–258 (1990).
119. Dabbousi, B. O. *et al.* (CdSe)ZnS Core–Shell Quantum Dots: Synthesis and Characterization of a Size Series of Highly Luminescent Nanocrystallites. *J. Phys. Chem. B* **101**, 9463–9475 (1997).
120. Mokari, T., Rothenberg, E., Popov, I., Costi, R. & Banin, U. Selective growth of metal tips onto semiconductor quantum rods and tetrapods. *Science* **304**, 1787–1790 (2004).
121. Shi, W. *et al.* A General Approach to Binary and Ternary Hybrid Nanocrystals. *Nano Lett.* **6**, 875–881 (2006).
122. Langille, M. R., Zhang, J., Personick, M. L., Li, S. & Mirkin, C. A. Stepwise evolution of spherical seeds into 20-fold twinned icosahedra. *Science* **337**, 954–957 (2012).
123. Scarabelli, L., Sánchez-Iglesias, A., Pérez-Juste, J. & Liz-Marzán, L. M. A ‘Tips and Tricks’ Practical Guide to the Synthesis of Gold Nanorods. *J. Phys. Chem. Lett.* **6**, 4270–4279 (2015).
124. Sibbald, M. S., Chumanov, G. & Cotton, T. M. Reduction of Cytochrome c by Halide-Modified, Laser-Ablated Silver Colloids. *J. Phys. Chem.* **100**, 4672–4678 (1996).

125. Pérez-Juste, J., Liz-Marzán, L. M., Carnie, S., Chan, D. Y. C. & Mulvaney, P. Electric-Field-Directed Growth of Gold Nanorods in Aqueous Surfactant Solutions. *Adv. Funct. Mater.* **14**, 571–579 (2004).
126. Fruton, J. S. Oxidation-reduction potentials of ascorbic acid. *J. Biol. Chem.* **105**, 79–85 (1934).
127. Near, R. D., Hayden, S. C., Hunter, R. E., Thackston, D. & El-Sayed, M. A. Rapid and Efficient Prediction of Optical Extinction Coefficients for Gold Nanospheres and Gold Nanorods. *J. Phys. Chem. C* **117**, 23950–23955 (2013).
128. Carbone, L., Jakab, A., Khalavka, Y. & Sönnichsen, C. Light-Controlled One-Sided Growth of Large Plasmonic Gold Domains on Quantum Rods Observed on the Single Particle Level. *Nano Lett.* **9**, 3710–3714 (2009).